

# Self-Organization and Maintenance of Simulated Nocturnal Convective Systems from PECAN

MATTHEW D. PARKER<sup>a</sup>

<sup>a</sup> North Carolina State University, Raleigh, North Carolina

(Manuscript received 13 August 2020, in final form 13 January 2021)

ABSTRACT: The Plains Elevated Convection at Night (PECAN) field project was designed to explain the evolution and structures of nocturnal mesoscale convective systems (MCSs) and relate them to specific mechanisms and environmental ingredients. The present work examines four of the strongest and best-organized PECAN cases, each numerically simulated at two different levels of complexity. The suite of simulations enables a longitudinal look at how nocturnal MCSs resemble (or differ from) more commonly studied diurnal MCSs. All of the simulations produce at least some surface outflow ("cold pools"), with stronger outflows occurring in environments with more CAPE and weaker nearground stability. As these surface outflows emerge, the lifting of near-ground air occurs, causing each simulated nocturnal MCS to ultimately become "surface-based." The end result in each simulation is a quasi-linear convective system (QLCS) that is most intense toward the downshear flank of its cold pool, with the classical appearance of many afternoon squall lines. This pathway of evolution occurs both in fully heterogeneous real-world-like simulations and horizontally homogeneous idealized simulations. One of the studied cases also exhibits a back-building "rearward off-boundary development" stage, and this more complex behavior is also well simulated in both model configurations. As a group, the simulations imply that a wide range of nocturnal MCS behaviors may be self-organized (i.e., not reliant on larger-scale features external to the convection).

KEYWORDS: Cold pools; Convective storms; Convective-scale processes; Mesoscale processes; Mesoscale systems; Cloud resolving models

## 1. Introduction

Nocturnal mesoscale convective systems (MCSs) contribute to a distinctive nighttime maximum in warm season precipitation in the central United States (Wallace 1975; Maddox 1980; Fritsch et al. 1986; Carbone et al. 2002). Historically, such nocturnal systems have been associated with lower predictability (Olson et al. 1995; Davis et al. 2003; Fritsch and Carbone 2004; Weisman et al. 2008; Peters et al. 2017; Stelten and Gallus 2017). Nocturnal MCSs were therefore a focus of the 2015 Plains Elevated Convection at Night (PECAN) field project (Geerts et al. 2017). PECAN MCS missions specifically targeted the evolution of MCS structures as well as their relationship to environmental ingredients and physical mechanisms.

Parker et al. (2020, hereafter P20) reviewed a range of historical nocturnal MCS studies; here we distill a few important themes. Because the nocturnal stable boundary layer (SBL) has decreased CAPE and increased CIN in comparison to the diurnal mixed layer, nocturnal MCSs are often assumed to be "elevated" (e.g., Colman 1990; Parker 2008), that is, to ingest air parcels that originate solely from above the SBL. However, a number of studies (Parker 2008; French and Parker 2010; Billings and Parker 2012) have shown that nocturnal MCSs may still

Corresponding author: Matthew D. Parker, mdparker@ncsu.edu

ingest air from the SBL (thereby making them "surface-based"). This distinction could have implications for the forecasting of nocturnal MCS's translational speeds as well as their production of severe winds and tornadoes. P20 simulated a nocturnal MCS from PECAN that produced severe winds within an environment that might customarily be associated with elevated convection. They found that both a full-physics case study simulation and an idealized simulation produced surface cold pools, which maintained the simulated MCSs and ultimately enabled them to ingest near-surface air.

Based on this progression, P20 concluded that the MCS was largely self-organized, meaning that its structure and evolution were primarily determined by a combination of the local preconvective environmental profile and the MCS's subsequent history of convectively generated features (e.g., cold pools, waves or bores, rear inflow jets), not by continued synopticscale lifting or external heterogeneity. Such self-organization of convection along surface outflow boundaries is a fundamental component of our understanding of squall lines (e.g., Newton 1950; Zipser 1977; Thorpe et al. 1982; Fovell and Ogura 1988; Rotunno et al. 1988). P20 went on to examine some aspects of severe wind production in the pair of simulations. But, perhaps the most consequential claim from P20 was that "nocturnal MCSs may often resemble their cold pool-driven, surface-based afternoon counterparts." There is at least some corroborating evidence for this in the observations

presented by Hitchcock et al. (2019); most PECAN MCS cases had surface cold pools (having a median surface temperature deficit of 5 K and a median depth exceeding 2 km).

The realism of the P20 idealized model simulation, and its similarity to their full-physics simulation, constituted the primary evidence for the hypothesis that nocturnal MCSs are largely self-organized. By emphasizing the role of convectively generated outflows, this hypothesis raises questions about the relative importance of external preexisting features (e.g., fronts, low-level jets, midtropospheric waves), which are present in nature and included in case study simulations (but omitted from idealized simulations). Given the wide spectrum of synoptic regimes associated with nocturnal convection in the warm season, it is important to determine whether the 25–26 June PECAN case might understate (or overstate) the typical importance of such external processes. Thus, the research question in this article is whether the self-organization hypothesis describes other nocturnal MCSs.

Our specific aim is to provide a more longitudinal look at the self-organization and maintenance of nocturnal MCSs using additional cases from PECAN. Such integrative studies are often a stated goal of field projects, but the day-to-day variability in data collection strategies tends to primarily facilitate the publication of individual case studies. Here we employ the general methods and analysis framework of P20, but apply them to three more of the strongest and best-organized cases from the 2015 PECAN field campaign (with a reprise of the P20 case, for a total of four). At least three of the four cases have received detailed study to date (as will be reviewed in section 3). Thus, the present work will focus not on a comprehensive description of the individual cases, but rather upon the common processes and evolution among an ensemble of simulations of the cases. The strength of this approach is in revealing the repeated behaviors that occur within a sample of eight nocturnal MCS simulations undertaken at two different levels of complexity.

Section 2 of this article recaps the model configurations used in this study (which are identical to those of P20). Section 3 provides a very brief overview of the four observed cases studied here, including how well both the case study and idealized simulations compare to the observations. Section 4 focuses on the common evolution of the simulated systems from initially elevated convection toward subsequently surface-based, cold pool–driven MCSs. The article concludes in section 5 by distilling the processes and ramifications of nocturnal MCS self-organization and maintenance that are depicted by these simulations.

#### 2. Methods

A pair of simulations is performed for each of four PECAN nocturnal MCS cases: 24–25 June 2015 ("IOP15"), 25–26 June 2015 ("IOP16"), 5–6 July 2015 ("IOP20"), and 12–13 July 2015 ("IOP27"). These cases are reviewed individually in section 3. They were selected from a larger number of well-sampled PECAN MCSs, prioritizing well-organized squall lines that were also credibly simulated in both model configurations (not all cases were). While four cases cannot describe the full range

of nocturnal MCSs, this subset represents a first logical step toward understanding some of the highest-impact systems targeted by PECAN.

The numerical methods are the same as employed by P20, and the remainder of this section is drawn from P20 with minor modifications (emphasizing only the most distinctive attributes of the experimental design). For each case, there is a "full-physics case study" simulation using the Advanced Research core of the Weather Research and Forecasting model (the "WRF-ARW"; Klemp et al. 2007; Skamarock and Klemp 2008; Skamarock et al. 2008) and an "idealized" simulation using the Bryan Cloud Model 1 (CM1; Bryan and Fritsch 2002; Bryan and Morrison 2012). The details of each model's settings are described in Table 1.

Notably, as in P20, different microphysical parameterizations were selected for the WRF and CM1 production runs. Although this choice weakens the direct comparisons between models, it was motivated by an extensive set of exploratory tests on PECAN cases; in terms of reflectivity structures and system evolution, the WRF simulations were more realistic overall when using the Thompson et al. (2008) scheme, whereas the CM1 simulations were more realistic overall when using the Morrison et al. (2009) scheme. As will be discussed later, the different microphysics parameterizations may account for some discrepancies<sup>1</sup> between the cold pools in the WRF versus CM1 simulations. In short, a slightly less controlled experiment was tolerated in exchange for greater correspondence between the simulations and the observed cases.

## a. WRF case study simulations

The "full-physics case study" simulations used version 3.6 of the WRF-ARW model. The simulations ultimately included four nested grids (details in Table 1), whose boundaries are shown for the respective cases in Figs. 1a, 1d, 1g, and 1j. The outermost 15 km domains were initialized at 0000 UTC on the day preceding the event of interest, which was more than 24 h before the development of the convective storms studied by PECAN. The 3 km domain was then launched after 18 h (at 1800 UTC), followed by the 1 km and 333 m domains after 24 h (at 0000 UTC on the day of the PECAN observations, but still several hours before the primary MCS developed). The physical parameterizations are summarized in Table 1, with convective motions treated explicitly on all grids except for the outermost 15 km domain. To assess the origins of air parcels in both the updrafts and outflows of simulated convective storms,

<sup>&</sup>lt;sup>1</sup> In preliminary tests comparing the Morrison versus Thompson microphysics parameterizations for these four cases in CM1, there was no systematic relationship between the choice of scheme and the cold pool strength. Nevertheless, the implementations of a given microphysical parameterization vary among numerical models, and they evolve independently with successive code releases (e.g., as each model's numerics change and as bugs are corrected). Thus, even with the same basic schemes, differences may still emerge between the models. Having prioritized production runs with greater overall similarity to observations, this study avoids detailed comparisons of the microphysical differences between models.

TABLE 1. Summary of model settings for the WRF (v. 3.6) and CM1 (v. 17) simulations in this article. The colloquial names for various parameterizations are given in the table, with corresponding literature citations as follows: "MYJ boundary layer scheme" (Mellor and Yamada 1982; Janjić 2002); "TKE-based subgrid closure" (Deardorff 1980; Bryan and Morrison 2012); "RRTM–Dudhia scheme" (Mlawer et al. 1997; Dudhia 1989); "Noah–Eta scheme" (Chen and Dudhia 2001); "Kain–Fritsch scheme" (Kain and Fritsch 1993; Kain 2004).

Setting	WRF simulation	CM1 simulation		
$\Delta x, \Delta y$	15–3–1 km, two-way nested	0.25 km		
	0.33 km, one-way nested			
Vertical levels	d01, d02, d03: 40	72		
	d04: 79			
$\Delta z$	$d01, d02, d03$ : stretched, $\approx 50-660 \text{ m}$	Stretched, 100–250 m		
	d04: stretched, $\approx$ 25–330 m			
Model top	≈20.5 km	16.5 km, with Rayleigh damping		
		above 14.0 km		
Microphysical parameterization	Thompson et al. (2008)	Morrison et al. (2009)		
Turbulence parameterization	MYJ boundary layer scheme	TKE-based subgrid closure		
Radiation parameterization	RRTM-Dudhia scheme	None		
Land surface parameterization	Noah-Eta scheme	None, free-slip bottom boundary		
Convective parameterization	Kain-Fritsch scheme (15 km grid only)	None		
Initialization	NAM model analysis	Horizontally homogeneous,		
	0000 UTC on previous day	with inserted line of four warm bubbles		
Lateral boundary conditions	NAM model analyses every 6 h	Open radiative condition		
Simulation time	Ending time 33 h (0900 UTC)	6 h		
	d01 33 h, d02 15 h, d03 9 h, d04 9 h			
Dynamical simplifications	None	Coriolis acceleration omitted		

passively advected tracers were introduced in 500-m-deep layers extending from the surface through 6 km AGL. Because the boundary layer parameterization caused the tracers to become heavily diluted (and no longer useful for assessing the origins of recently ingested air), the 30 min tracer reset procedure described by P20 was again employed.

## b. CM1 idealized simulations

The "idealized" simulations used version 17 of the CM1 model. These simulations used far fewer parameterizations (Table 1), with the intention of providing a simpler framework for physical attribution, and isolating the aspects of the simulated MCSs that were self-generated. The initial model environments were horizontally homogeneous, each given by a single sounding and wind profile (these soundings are described further in section 3). The CM1 simulations presented here were initialized with a sounding taken from just ahead of each MCS. For three of the four cases, this was an observed sounding from PECAN; ultimately, as discussed by P20, a WRF gridpoint sounding had to be used for the IOP16 case. One of the soundings (for the IOP15 case) also had a layer that required trivial wind modifications to remove Kelvin-Helmholtz instability. Passive tracers were again added to the initial conditions in the lower-middle troposphere (and did not require the periodic resetting used in the WRF simulation).

Whereas the WRF simulations can generate deep convection organically via synoptic and mesoscale processes, the CM1 simulations cannot. Instead, a line of four warm bubbles (with the same properties as described by P20) was introduced into the CM1 model at the initial time of each simulation. P20 showed that their IOP16 CM1 simulation was largely insensitive to the initial orientation of their line of warm bubbles; they cited this as

strong evidence that the convection was self-organizing (in other words, not preordained by the initial lifting that triggered it). In an attempt to mirror the P20 experimental design and determine the generality of their results, all four cases were simulated with an initial north–south line orientation. However, the IOP27 simulation proved to require an initial east–west orientation to produce realistic results, and those are the results presented herein. This may mean that in some cases self-organizing processes are more sensitive to the initial patterns of convective initiation (which would imply at least an indirect role for larger-scale lifting).

#### 3. Overview of observed cases and simulations

The four cases selected for this study have several attributes in common. Each case was well-sampled by the PECAN project, and produced a credible simulation in the WRF and CM1 modeling frameworks. Each case included a well-organized linear MCS (a quasi-linear convective system, or "QLCS") within an environment where there was a lower-tropospheric stable layer and the largest CAPE and smallest CIN values resided above the surface. Finally, each case was also associated with at least some severe surface winds (ranging from 9 to 144 total local storm reports). By happenstance, the progression of the cases from IOP15 to IOP27 corresponds to environments that would also be progressively more favorable for surface-based convection; thus, the suite of four cases represents a spectrum of possible summertime nocturnal MCS environments.

Within this longitudinal, simulation-focused article, there is not room to also provide a detailed analysis of the observations from each PECAN case. In this section a brief overview for each case is followed by a comparison to its associated pair of

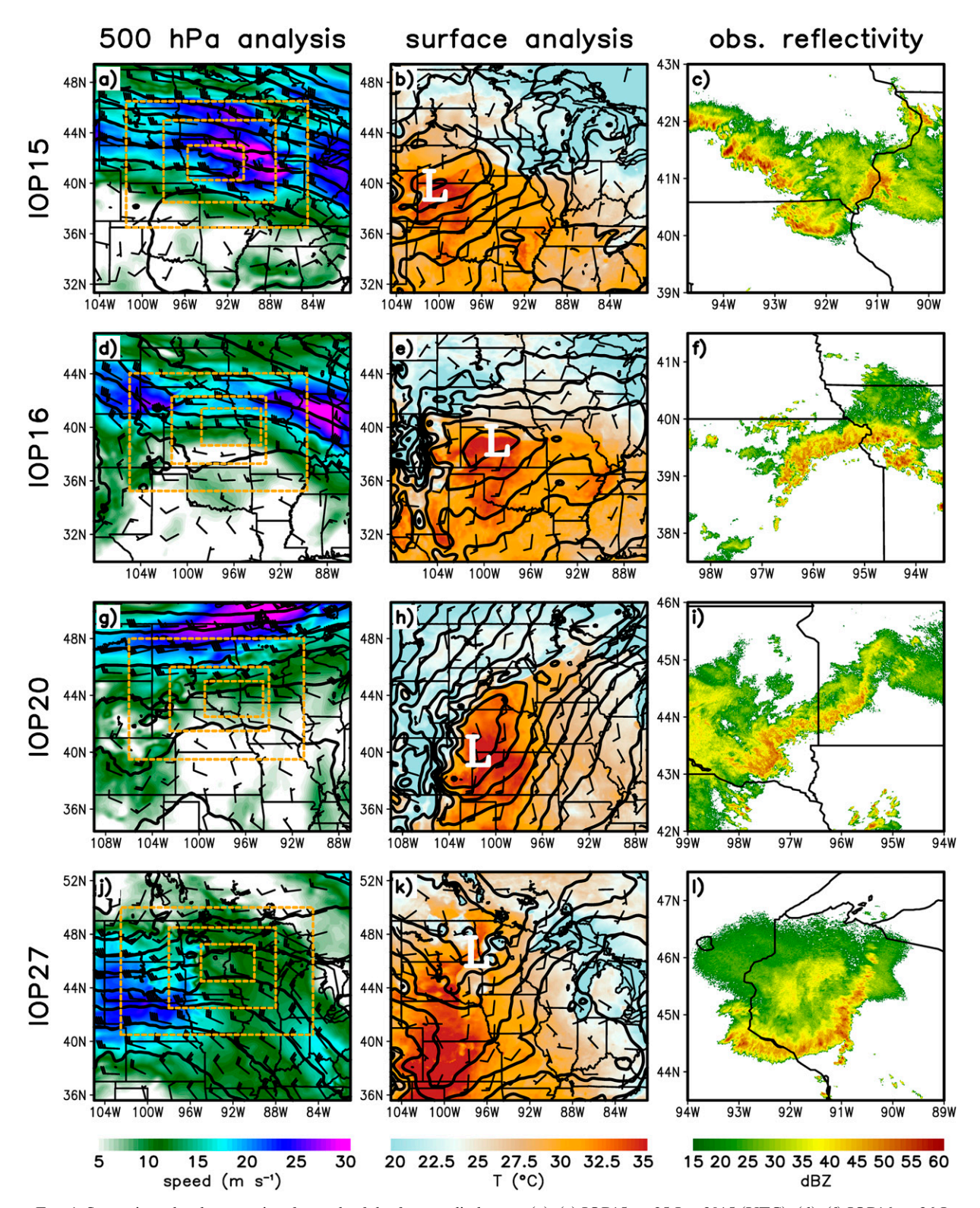


FIG. 1. Synoptic and radar overview for each of the four studied cases: (a)–(c) IOP15 on 25 Jun 2015 (UTC), (d)–(f) IOP16 on 26 Jun 2015 (UTC), (g)–(i) IOP20 on 6 Jul 2015 (UTC), and (j)–(l) IOP27 on 13 Jul 2015 (UTC). (left) 500 hPa heights (contours, in m), wind barbs (barb =  $5 \text{ m s}^{-1}$ , flag =  $25 \text{ m s}^{-1}$ ), and isotachs (shaded, in m s $^{-1}$ ), plotted from the WRF 15 km model domain valid at 0000 UTC on the day given above. The extents of the WRF nested grids (3 km, 1 km, and 333 m grid spacing) are indicated with dashed orange boxes. (center) Surface pressure reduced to mean sea level (contours, in hPa), wind barbs (barb =  $5 \text{ m s}^{-1}$ ), and temperature (shaded, in °C),

simulations. The case summaries provide context; however, the primary analysis in the remainder of this article focuses only on the simulations. The expectation for these simulations is not exact reproduction of the observed cases, but rather sufficiently representative baselines to enable the larger longitudinal comparison.

## a. 24-25 June 2015 (IOP15)

The first studied case occurred primarily in Iowa on 24-25 June (PECAN IOP15; Fig. 1c). A preexisting stationary front was situated beneath an upper-tropospheric jet streak (Figs. 1a,b), although there was not a clearly defined uppertropospheric trough. Such a scenario might be characterized as having moderately strong synoptic-scale lifting in the context of summer. Among the four studied cases, IOP15 had the environment that would most typically be expected to support elevated convection (e.g., Fig. 2); the lowest few hundred meters had CAPE  $< 500 \,\mathrm{J\,kg^{-1}}$  (Fig. 3a) and CIN magnitudes exceeding 250 J kg<sup>-1</sup> (Fig. 3b), which would require air parcels to be lifted in excess of 2.5 km to reach their LFCs (the quantity "\Delta z<sub>LFC</sub>"; Fig. 3c). Late afternoon/early evening convection developed along and on the cool side of the stationary front in central Iowa where low-level southerlies overran it; in time, more convection developed into southeastern Iowa. In addition to a southeastward-moving bowing segment, a region of rearward off-boundary development (ROD; Peters and Schumacher 2014) occurred, with continued backbuilding of quasi-stationary convection extending northwestward from the bow echo (Fig. 1c); this gave the system a structure reminiscent of the "bow and arrow" archetype identified by Keene and Schumacher (2013). The forward propagating bowing segment of the IOP15 MCS was associated with nine severe wind reports. Meanwhile, the ROD segment produced flash flooding, with widespread rainfall in excess of 75 mm (and three reports in excess of 150 mm). More information about IOP15 can be found in the detailed studies of Peters et al. (2017) and Hitchcock and Schumacher (2020).

The defining characteristics of the IOP15 case (Fig. 1c) were a southeastward-moving bowing segment along with a backbuilding ROD segment producing convection that extended northwestward behind the leading bow echo. Both the WRF case study (Figs. 4a,b) and CM1 idealized (Figs. 4c,d) runs capture this combination of the southeastward-moving line as well as the loosely arranged region of convection that trails off toward the northwest. A version of this IOP15 WRF simulation was further analyzed and discussed by Peters et al. (2017), who showed that the exact placement of the ROD segment is quite sensitive to the environmental lower-tropospheric humidity. It is therefore rather remarkable that the idealized framework is capable of producing this region of ROD backbuilding convection. This successful

resemblance may in turn be an indicator that the ROD structure is largely self-organized by the MCS itself. More details of how such structures occur in a simulation like this one are provided by Hitchcock and Schumacher (2020), whose work was also derived from IOP15.

# b. 25-26 June 2015 (IOP16)

The second studied case occurred primarily in Kansas and Missouri on 25-26 June (PECAN IOP16; Fig. 1f). The general setting was a preexisting stationary front with an approaching upper-tropospheric trough (Figs. 1d,e); the MCS developed within the moderate midlevel flow between two jet streaks. Such a scenario could again be characterized as having moderately strong synoptic-scale lifting in the context of summer. The IOP16 environment might commonly be thought to support elevated convection; its lowest 1 km AGL has lower CAPE, considerably more CIN, and much greater  $\Delta z_{LFC}$  in comparison to air parcels residing farther aloft (Fig. 3). A representative observed preline sounding from PECAN is shown in Fig. 2b. However, as described by P20, for the CM1 simulation of this case (and this case only), a gridpoint sounding from the WRF model was used for the initial condition; P20 established the similarity of the WRF sounding to the observations, and discussed the strengths and weaknesses of this approach. A number of embedded bowing segments developed (somewhat visible in Fig. 1f) that ultimately produced 43 severe wind reports, including 5 significant severe wind reports. More information about IOP16 can be found in the detailed studies of Degelia et al. (2019), Miller et al. (2020), and P20.

The defining characteristics of the IOP16 case included a line of storms moving southeastward with embedded bowing segments (Fig. 1f). The WRF case study simulation (Figs. 4e,f) produces very similar structures to the observed case, albeit with some net displacement to the north. The CM1 idealized simulation (Figs. 4g,h) produces a northeast–southwest oriented convective line that moves southeastward and produces embedded bowing segments. However, as discussed by P20, there is spurious convection that extends off toward the north and northwest in the idealized simulation, which is due to the fact that in the horizontally homogeneous model environment there is no poleward decline in instability. P20 performed analysis of this pair of simulations while ignoring the spurious northern extent of the CM1 MCS.

## c. 5-6 July 2015 (IOP20)

The third studied case occurred primarily in South Dakota and Minnesota on 5–6 July (PECAN IOP20; Fig. 1i). A weak midtropospheric shortwave trough crossed the Rockies (Fig. 1g) and was associated with a lee cyclone centered in southwestern Nebraska as well as a southward moving cold front in the Northern Plains (Fig. 1h); although the midtropospheric

 $\leftarrow$ 

plotted from the WRF 15 km model domain valid at 0000 UTC on the day given above. (right) Observed logarithmic radar reflectivity (shaded, in dBZ), valid for the following times and radar locations on the day given above: (c) 0528 UTC, Davenport, IA; (f) 0605 UTC, Topeka, KS; (i) 0527 UTC, Sioux Falls, SD; (l) 0601 UTC, La Crosse, WI.

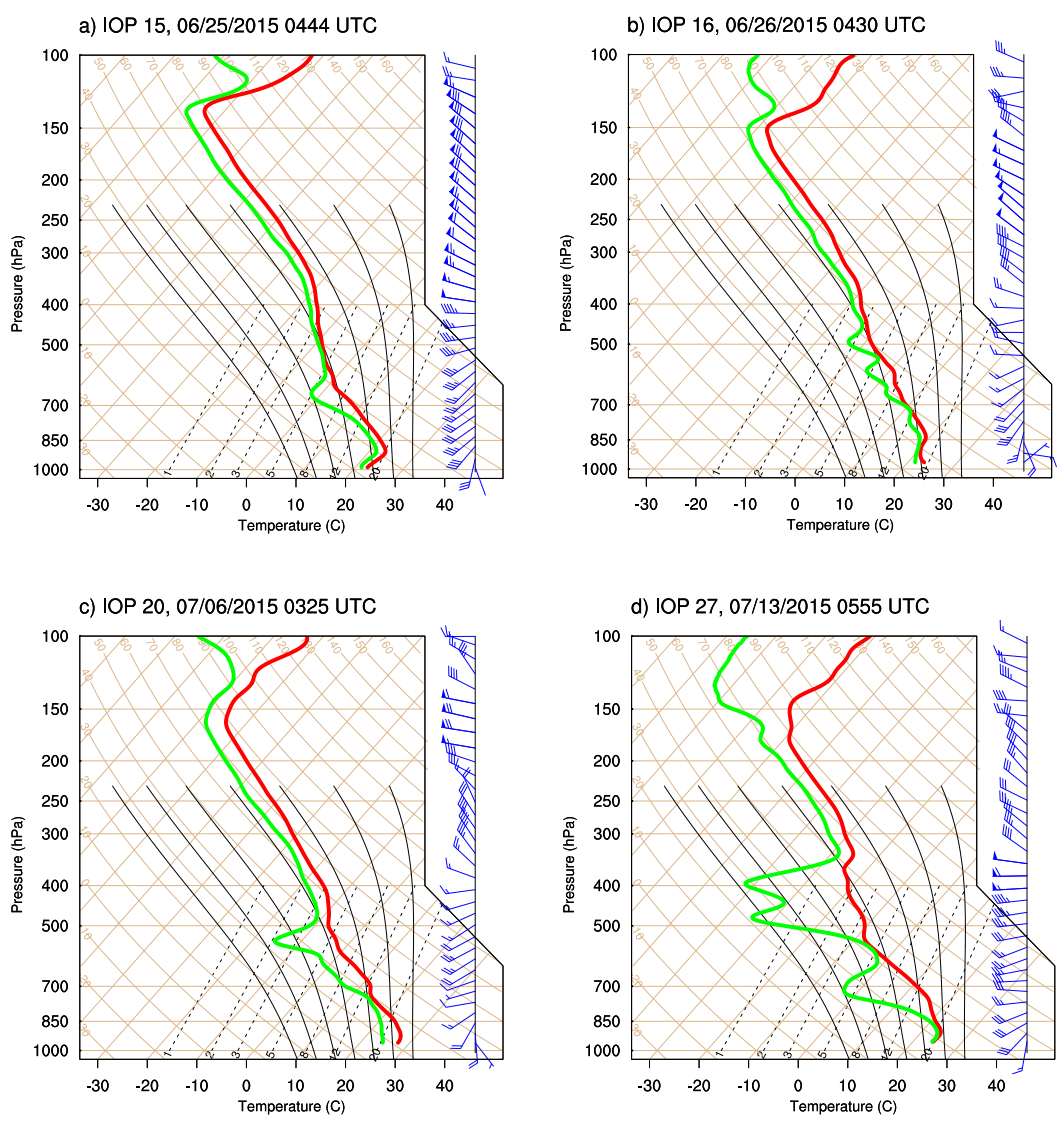


FIG. 2. Skew T-logp diagram of observed temperature, humidity, and wind barbs (barb = 5 m s<sup>-1</sup>, flag = 25 m s<sup>-1</sup>) for the four events (as labeled above) described in this study. Each sounding was the last available PECAN sounding prior to the arrival (or substantial contamination by) the mature, targeted MCS. The soundings were passed through a simple vertical smoother (the same procedure used by Parker 2014) to remove noise before plotting. Vertical profiles of CAPE, CIN, and  $\Delta z_{\rm LFC}$  for these soundings are shown in Fig. 3.

disturbance and flow were rather weak, the frontal lifting for this case might be characterized as unseasonably strong. Despite being nocturnal, this environment would generally be considered more favorable for convection rooted in the boundary layer, with substantial surface-based CAPE, as well as much less CIN and smaller  $\Delta z_{\rm LFC}$  than either IOP15 or IOP16 (Fig. 3). Convection developed in the High Plains of western Nebraska and South Dakota and grew upscale into a well-organized MCS, while new nocturnal convection also formed along the southward-moving cold front in eastern South Dakota and western Minnesota. A number of embedded bowing segments (Fig. 1i) associated with mesovortices ultimately produced 21 severe wind reports as well as a weak

tornado. More information about IOP16 can be found in the detailed studies of Bodine and Rasmussen (2017), Flournoy and Coniglio (2019), and Chipilski et al. (2020).

The defining characteristics of the IOP20 case were a pair of lines (or arcs) of convection that intersected in South Dakota (Fig. 1i): a north–south segment that originated from earlier convection over the High Plains of Nebraska and South Dakota as well as a northeast–southwest segment that originated along the cold front that was moving southward through Minnesota and South Dakota. These structures were captured quite faithfully by the WRF case study run (Figs. 4i,j). Understandably, in the idealized CM1 simulation (where convection is initiated with a single line of warm bubbles) there

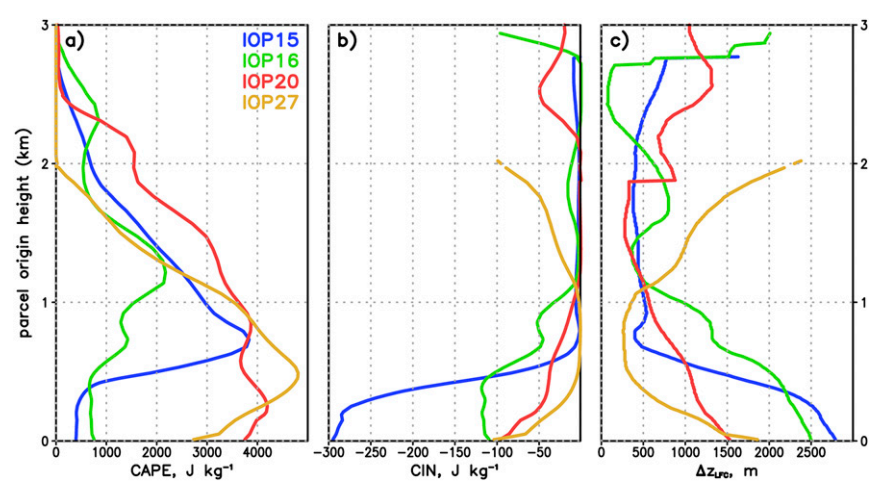


FIG. 3. (a) CAPE, (b) CIN, and (c) required lifting depth ( $\Delta z_{\rm LFC}$ ) as a function of a parcel's original level. CIN and  $\Delta z_{\rm LFC}$  are only plotted for parcels with CAPE  $> 0\,{\rm J\,kg}^{-1}$  (where CAPE  $= 0\,{\rm J\,kg}^{-1}$  the data are masked). All data from the IOP 15 (0444 UTC 25 Jun 2015) PECAN observation are plotted in blue. All data from the IOP16 (0430 UTC 26 Jun 2015) PECAN observation are plotted in green. All data from the IOP20 (0325 UTC 6 Jul 2015) PECAN observation are plotted in red. All data from the IOP27 (0555 UTC 13 Jul 2015) PECAN observation are plotted in dark yellow. The original skew T-logp profiles for these soundings are shown in Fig. 2.

is no separate history of two distinct merging lines; however, the primary feature of a northeast–southwest-oriented squall line that moves southeastward is indeed reproduced.

## d. 12-13 July 2015 (IOP27)

The fourth studied case occurred primarily in Minnesota and Wisconsin on 12-13 July (PECAN IOP 27; Fig. 11). This case had the least supportive synoptic setting of the four considered here, with modest midtropospheric flow and only a weak midtropospheric jet streak to the west of the area where the MCS formed (Fig. 1j). At the surface, an extremely weak stationary front extended from North Dakota through Indiana, but with a negligible temperature gradient and wind shift (Fig. 1k). Although CAPE was maximized above the surface, this environment had ample CAPE both at the surface and aloft, with the least mean CIN and the smallest mean  $\Delta z_{\rm LFC}$  in the 0-1 km layer among the four cases (Fig. 3). To the extent that a surface stationary front could be analyzed, convection developed along and to its cool side. Storms quickly became organized into a line that was oriented perpendicular to the front and moved parallel to it, toward the southeast (Fig. 11). The MCS survived for a period of nearly 24 h, ultimately dissipating near the Appalachian Mountains of West Virginia, Virginia, and North Carolina; during the overnight hours of 13 July, it produced 144 severe winds reports across Minnesota, Wisconsin, and Illinois. This MCS has to date been the least studied among the four cases presented here, although it was included among the numerical simulations performed by Thielen and Gallus (2019).

The defining characteristic of the IOP27 case was a single primary squall line oriented almost east—west and moving south-southeastward through Wisconsin (Fig. 11). This is well captured in the WRF case study simulation (Figs. 4m,n).

The convection in the idealized CM1 simulation is slow to develop, but it does eventually produce a large, correctly oriented arc-shaped MCS that moves southeastward.

## e. Synthesis

In general, the WRF case study simulations credibly represent the system-scale structures of the observed cases. The CM1 simulations depart much more noticeably from the observations. Such departures are not surprising given the horizontally homogeneous initial conditions as well as the neglect of a number of physical parameterizations (especially radiation and surface fluxes). But, the difference in configurations of the WRF and CM1 models provides an important basis for understanding the degree to which MCS evolution is self-organized (the only form of evolution possible in the idealized CM1 runs) versus driven by factors external to the MCS (environmental evolution and heterogeneity, large-scale lifting, etc.). Although severe wind production is not an emphasis of the present article, it is noteworthy that all of the simulations produced peak surface winds surpassing the 26 m s<sup>-1</sup> threshold for severe thunderstorm gusts (each exceeded 31 m s<sup>-1</sup>; not shown). This is consistent with the severe wind reports reviewed above, and lends credence to the idea that these MCSs may have had appreciable surface outflows. In all, the IOP15 case had the clearest resemblance to an elevated MCS (in terms of its environment and evolution) whereas the IOP27 case had the clearest resemblance to a surface-based MCS. The varying synoptic setting, lower-tropospheric stability, and convective parameters make these cases a very instructive suite for the longitudinal modeling study.

To an extent, the CM1 simulations all produce MCSs that resemble one another (Fig. 4). This is in part due to the simple initial trigger for the convection, and in part due to

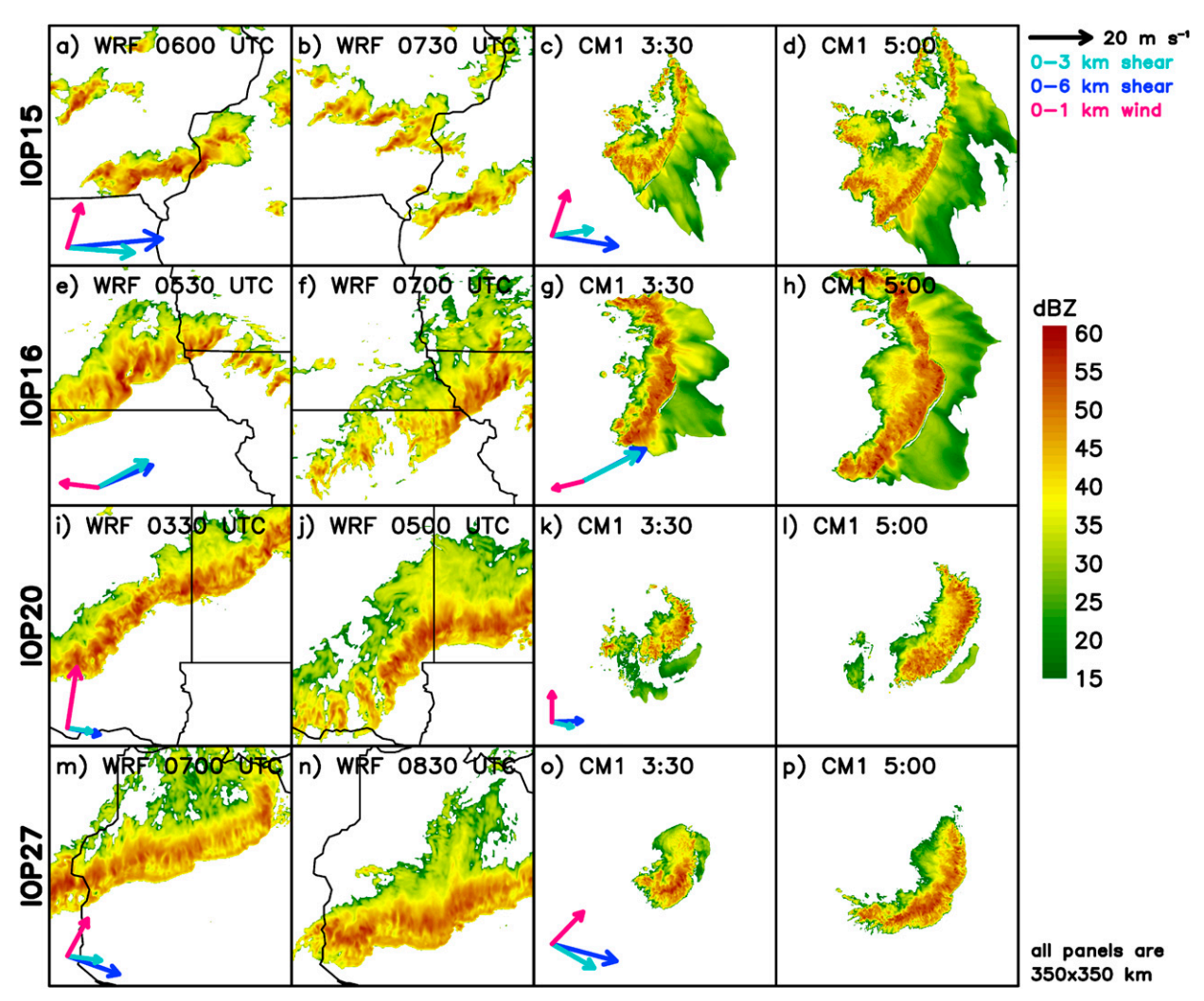


FIG. 4. Simulated logarithmic radar reflectivity factor (dBZ) at the surface from the 1-km domain of the (left two columns) WRF simulations and (right two columns) from the CM1 simulations, for (a)–(d) IOP15, (e)–(h) IOP16, (i)–(l) IOP20, and (m)–(p) IOP27. All panels show a plot area of  $350 \times 350 \, \mathrm{km}^2$ . WRF simulations are labeled in UTC with U.S. state borders shown for reference. CM1 simulations are labeled by elapsed time. For reference, in the first and third columns for each case the environmental 0–3 km vector wind difference (light blue), 0–6 km vector wind difference (dark blue), and 0–1 km mean wind (magenta) vectors are plotted (in m s<sup>-1</sup>, scaled as shown in the upper right). These vectors represent averages over a  $0.5^{\circ} \times 0.5^{\circ}$  area ahead of the MCS in WRF and the initial base state environments in CM1.

the somewhat similar vertical wind profiles among the four cases (e.g., Fig. 2). While constituting only a subset of the possible parameter space, such wind profiles are quite representative of those observed during PECAN, with the four present cases and six other well-sampled MCS cases in Fig. 5 typically having a southerly low level jet below 1 km AGL, followed by veering from southwesterly winds at 1 km AGL to westerly winds at and above 3 km AGL. This description also matches most of the PECAN profiles studied by Hitchcock et al. (2019) that fell into their "potentially neutral + jet" and "elevated instability" classifications (which accounted for the preponderance of soundings made near mature MCSs, especially after 0300 UTC). Overall, while this study cannot claim to span the entire spectrum of wind profiles within which

nocturnal MCSs might occur, it does exemplify a range of MCS behaviors within the scope of what repeatedly occurred during PECAN.

In this respect, the similarity among the CM1 simulations suggests that they are an excellent baseline for how convection would evolve due solely to its local environment (i.e., without any influence from larger-scale features). From here on, we directly compare processes in the case study versus idealized frameworks (without continued reference back to the observations) in order to assess the degree to which the simulated structures and evolution can be explained in terms of processes that are external to (i.e., large-scale features in the WRF) versus internal to the MCSs. We also seek to determine the extent to which the simulated nocturnal systems are afternoon-like

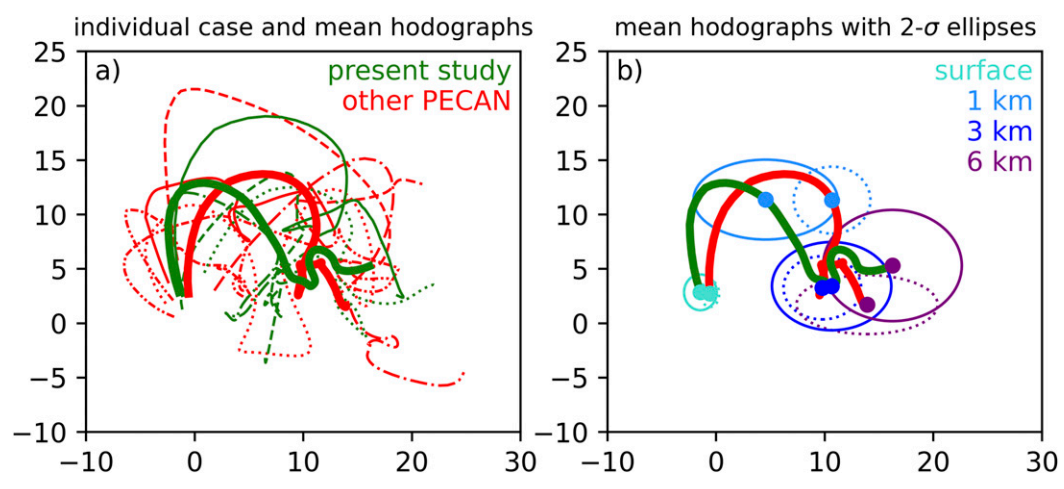


FIG. 5. Hodographs from 0 to 6 km AGL for the four cases in this study (plotted in green) and six other well-sampled MCS cases from PECAN (plotted in red; the cases were during 10–11 Jun, 16–17 Jun, 1–2 Jul, 8–9 Jul, 14–15 Jul, and 15–16 Jul 2015). Thick solid lines denote means of the four present cases (green) and the six other cases (red) in both panels. (a) Each case is given its own line style to aid in distinguishing them (the line styles have no other meaning). (b) Heights are indicated on the mean hodographs via colored dots (keyed as shown), and an ellipse is drawn (in the same color) to encircle two standard deviations around each mean. The solid ellipses correspond to the present study (green) mean profile and the dashed ellipses correspond to the other PECAN cases (red) mean profile.

(i.e., possessing surface cold pools and ingesting air from near the surface), as proposed by P20.

#### 4. Simulated structures and evolution

The gross similarity between the reflectivity structures in the CM1 simulations and their WRF counterparts motivates a closer comparison of the mechanisms at work. Is self-organization occurring in these simulations? If so, what are the key processes governing it, and are they the same in the CM1 and WRF simulations? To address these questions, we examine both the horizontal and vertical structures of each simulated MCS.

In their study of IOP16, P20 found that early convection led to wavelike structures in the lower-tropospheric stable layer, which initially appeared to maintain the simulated QLCSs. Over time, they found that surface cold pools slowly developed as regions with the heaviest precipitation were associated with the descent of evaporatively cooled midlevel air with low equivalent potential temperature ( $\theta_e$ ). P20 further found that, as the surface cold pools developed and intensified, the simulated MCSs began to lift appreciable near-surface air into their mid- and upper-tropospheric updrafts (in other words, they became "surface based").

An overview of the present simulations reveals that both the WRF and CM1 realizations for all four cases produce at least modestly cooled outflow at the surface (Fig. 6a), and eventually lift surface air into their deep updrafts (Fig. 6b). The common structures developed among the eight simulations, taken alongside the legacy of many studies linking QLCS selfmaintenance to outflows (in the form of cold pools, gravity waves, and bores), motivate a focus upon the system-scale properties of the simulated outflows. Thereafter, we examine the vertical structures of the MCSs via cross sections through their most intense segments.

We select a time during the maturity of each simulated MCS (Fig. 7) for closer study; by these times, each simulated MCS has a surface cold pool and is ingesting surface air (cf. Fig. 6). Because each WRF simulation has a different time of convective initiation, varying key times are selected when both 1) the MCS has a structure representative of its mature phase, and 2) 25 min have elapsed since the most recent WRF tracer reset procedure (as explained in section 2). Generally, the cold pools are slower to develop in CM1 than in WRF. Without large-scale lifting, the CM1 systems have to undertake the comparatively inefficient process of bootstrapping from a small initial line of warm bubbles to a mesoscale cold pool. Since this source of early difference cannot be totally eradicated,  $t = 4 \text{ h} \cdot 0 \text{ min}$  is chosen as the key time for all four CM1 simulations to provide a uniform perspective on the comparative speed of MCS development across cases.

## a. Lower-tropospheric outflow structures

Plan views of surface potential temperature deficit reveal the substantial horizontal footprint of the simulated outflows (Fig. 8). The IOP15 cold pools are the least expansive (Figs. 8a,b), which is probably not surprising given that environment's strong stability and high relative humidity in the lower troposphere (limiting the potential for evaporative cooling; Fig. 2a). Indeed, the PECAN observations of IOP15 revealed only a weak surface cold pool with a potential temperature deficit of -1.9 K, as compared to observed deficits in the other cases of -2.9 K (for IOP16), -7.0 K (for IOP20), and -7.2 K (for IOP27; Hitchcock et al. 2019). Cold pool depths also vary dramatically among the eight simulations (Fig. 9). As above, depth again reveals that IOP15 is associated with the weakest (shallowest) cold pools (Figs. 9a,b). In contrast, the IOP20 and IOP27 simulations produce cold pool depths that match or exceed the previously studied IOP16, peaking at greater than

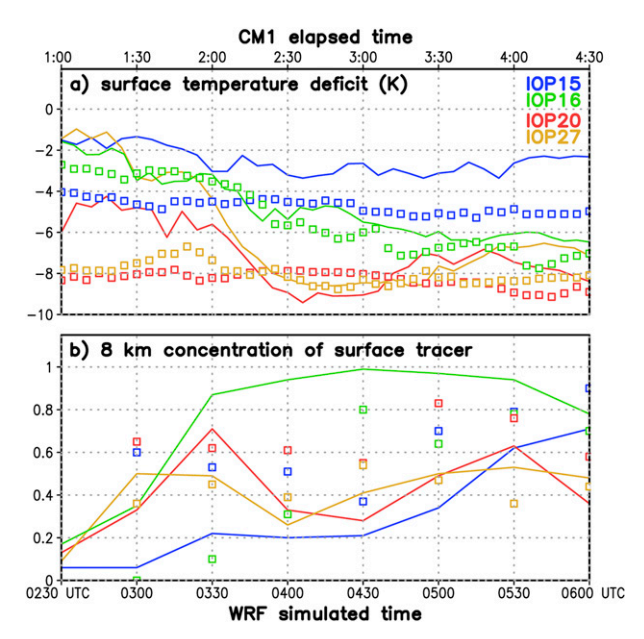


FIG. 6. History of (a) maximum surface cold pool temperature deficit and (b) maximum concentration of the 0–500 m tracer found at 8 km AGL, from the 333 m domain of the WRF simulations (open squares) and from the CM1 simulations (solid lines). WRF simulations are labeled in UTC (bottom abscissa), whereas CM1 simulations are labeled by elapsed time (top abscissa). Maxima for the WRF simulation are for a  $100 \times 150 \, \mathrm{km^2}$  area following the most intense part of the MCS (to remove spurious values related to far-field heterogeneity); maxima for the CM1 simulation are for the entire model grid. The tracer values are plotted at a half-hour interval in order to mask the repeated 30 min reset cycle undertaken in the WRF simulations (explained in section 2a).

1.5 km (Figs. 9c-h). Notably, Fig. 9 utilizes the more conservative of the two cold pool depth calculations from P20, which is the height of the ambient surface potential temperature surface. When using a more liberal definition of depth (the layer with negative buoyancy, i.e.,  $\theta' \leq -2$  K), P20 arrived at cold pool depths exceeding 4 km in the IOP16 simulations. Such deep layers of negative buoyancy are visible in the cross sections presented in section 4b (see Figs. 12–16), putting them in line with previously described depths for afternoon cold pools (e.g., Bryan and Parker 2010).

The WRF simulations generally have stronger cold pools than their CM1 counterparts, particularly in terms of their temperature deficits<sup>2</sup> and horizontal areas (left versus right columns in Fig. 8). The WRF cold pools do not necessarily have greater maximum depths than the CM1 cold pools (right vs left columns in Fig. 9), but the regions of substantial depth are again more extensive. Theoretically, a particular case's environment should support the same quasi-steady cold pool characteristics in both models; but the MCSs do not realize this mature state instantaneously (e.g., the downward trends evident in Fig. 6a). Rather, cold pool development is governed by the lower-tropospheric cooling rate and the amount of time over which it is applied. The cooling rate is no doubt influenced by the microphysical parameterization, which varied between the models (as described in section 2) and conceivably could have caused differences. Beyond this, the WRF systems have a longer history with more widespread convection due to the presence of synoptic lifting (e.g., by a frontal boundary), which increases both the elapsed time and horizontal footprint of cold pool production in comparison to the CM1 systems. In terms of the present analyses this means that the present CM1 simulations may actually understate the degree of MCS self-organization via

As discussed for IOP16 by P20, the simulated cold pools do not appear to form solely from in situ cooling in the near-surface layer. Instead, the air in the surface cold pools has much lower  $\theta_e$  than the ambient environment (Fig. 10), which indicates origins from farther aloft. An accompanying signature of the descent of lower- $\theta_e$  air to the surface is the displacement of surface tracer from those locations. This is clearly evident in the present simulations (Fig. 11), where the pockets of lowered  $\theta_e$  overlay pockets of near-zero surface tracer. This displacement is particularly evident in the CM1 simulations (right column in Fig. 11), wherein there is no periodic tracer reset procedure (in the WRF simulations, the surface tracer is reset to 1.0 every 30 min, so the footprint of midlevel air displacing the surface tracer is much more limited).

IOP15 is noteworthy again in that it has substantial  $\theta_e$  deficits (Figs. 10a,b) and widespread displacement of surface tracer (Figs. 11a,b) despite that fact that the surface air is not particularly cold (Figs. 8a,b). In other words, the basic process in IOP15 appears to mirror that in the other cases, but it does not result in air that is much cooler than ambient; this is discussed more later and is also described by Hitchcock and Schumacher (2020). The other case with distinctive cold pool traits is IOP20. In its preconvective environment,  $\theta_e$  is  $\geq 360 \,\mathrm{K}$  in the lowest 1.5 km AGL (and nearly constant in height, not shown), above which it declines to a minimum of 328 K at 4.5 km AGL. The widespread  $\theta_e$  values near 350 K in the IOP20 cold pools (Figs. 10e,f) represent smaller surface  $\theta_e$  deficits than occur in the other cases, implying that a smaller share of the cold pool's volume originated from midlevels. This may have resulted from the lower near-ground relative humidity in IOP20 (e.g., the dewpoint depressions visible in Fig. 2c), which would enable a greater proportion of the system's evaporative cooling to occur near the surface.

A natural question is whether the eight simulations' cold pools are able to lift near-surface air past its LFC and into deep convective updrafts. The blue contours in Fig. 11 reveal that all eight of the simulations have surface tracers present in their updrafts within the 5–10 km AGL layer. Interestingly, for

<sup>&</sup>lt;sup>2</sup> Pockets of surface warming are also evident to the rear of the MCSs, especially in the CM1 simulations. This warming is primarily due to regions of unsaturated descent in the presence of the lower-tropospheric stable layers, and is more noticeable in the less-mature, less-extensive CM1 systems. In addition, the somewhat crude way of computing potential temperature perturbations (using a single value for the preconvective environment) in the WRF means that larger-scale thermal gradients are also revealed in the plan views. However, such signals are typically weak in comparison to the pronounced convective cold pool structures seen in Fig. 8.

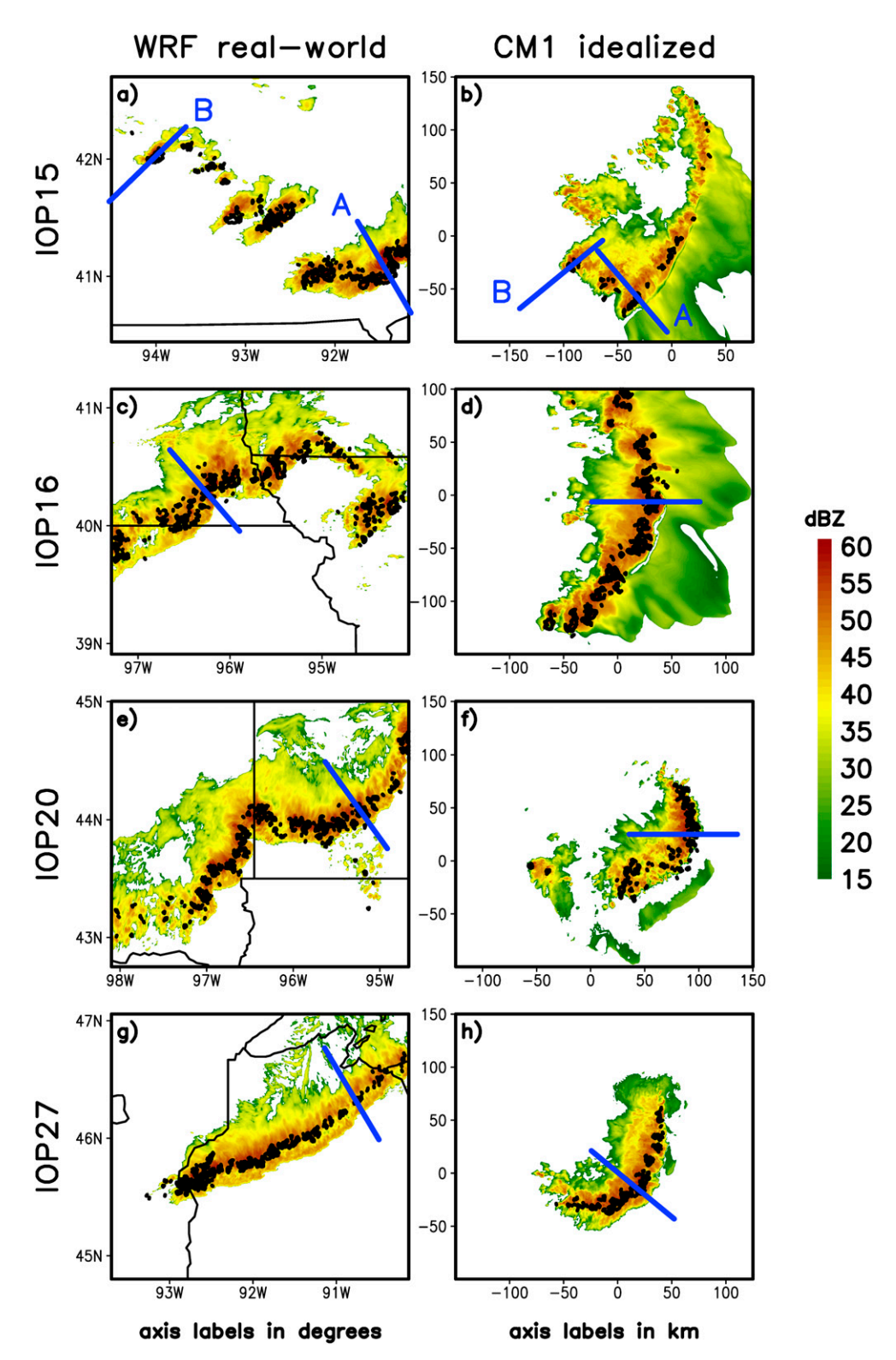


FIG. 7. Simulated logarithmic radar reflectivity factor (dBZ) at the surface and 8 km AGL vertical velocity (contoured in black at  $10 \text{ m s}^{-1}$ ) for key times that are analyzed in Figs. 8–16. One key time is chosen from each simulation for (a),(b) IOP15; (c),(d) IOP16; (e),(f) IOP20; and (g),(h) IOP27. (left) WRF plots are from the 333 m domain and are valid at (a) 0525, (c) 0555, (e) 0455, and (g) 0725 UTC. (right) All CM1 plots are valid at t=4 h 0 min elapsed time. The positions of the vertical cross sections in Figs. 12–16 are shown with blue line segments in each panel. All panels show a plot area of 250 (north–south)  $\times$  275 (east–west) km². WRF axes are labeled with latitudes and longitudes; CM1 axis labels are in km.

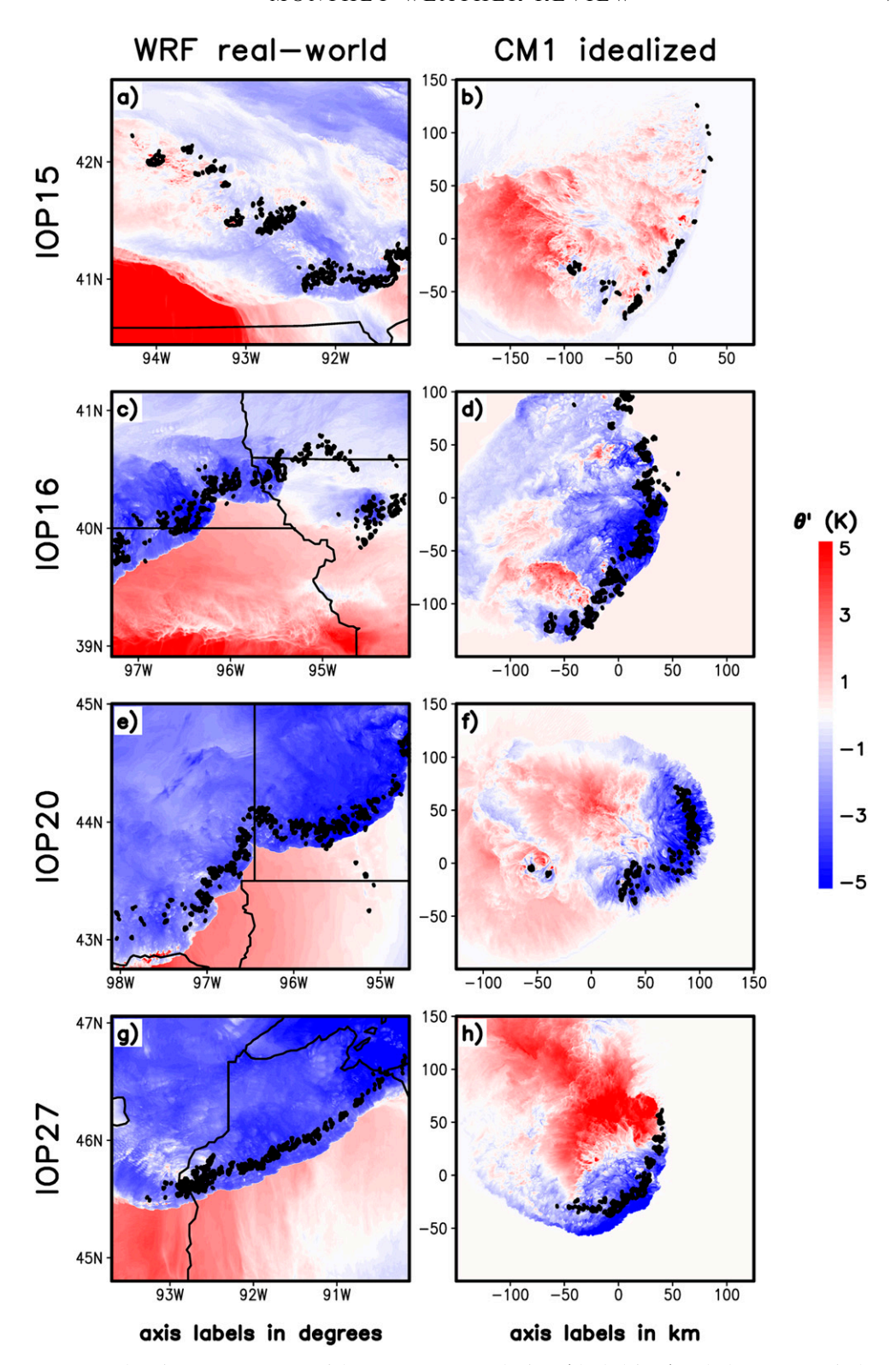


FIG. 8. Plan view of surface potential temperature perturbations (shaded, in K) and  $8\,\mathrm{km}$  AGL vertical velocity (contoured in black at  $10\,\mathrm{m\,s^{-1}}$ ). Perturbations are deviations from a single representative base-state value for each particular case (IOP), applied identically to the WRF and CM1 simulations for that case. All panels are valid for the same areas and times as their counterparts in Fig. 7.

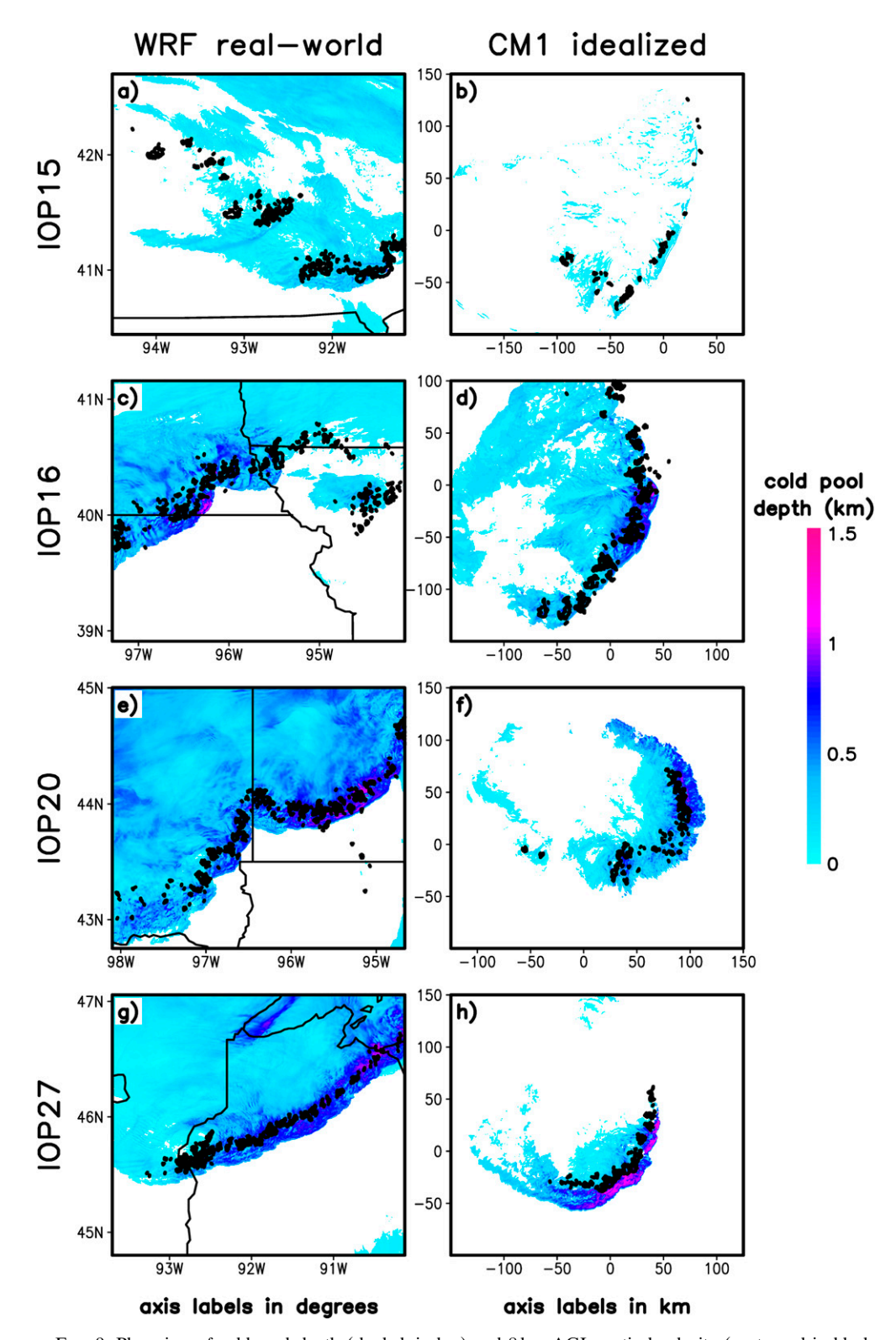


FIG. 9. Plan view of cold pool depth (shaded, in km) and  $8\,\mathrm{km}$  AGL vertical velocity (contoured in black at  $10\,\mathrm{m\,s^{-1}}$ ). The cold pool is represented by the depth of the layer with potential temperature less than the ambient surface value (in other words, this is the height of the surface isentrope). It is required that the cold pool condition be met in an uninterrupted layer extending upward from the surface, or else the value is masked (thus waves and bores are not shaded). All panels are valid for the same areas and times as their counterparts in Figs. 7 and 8.

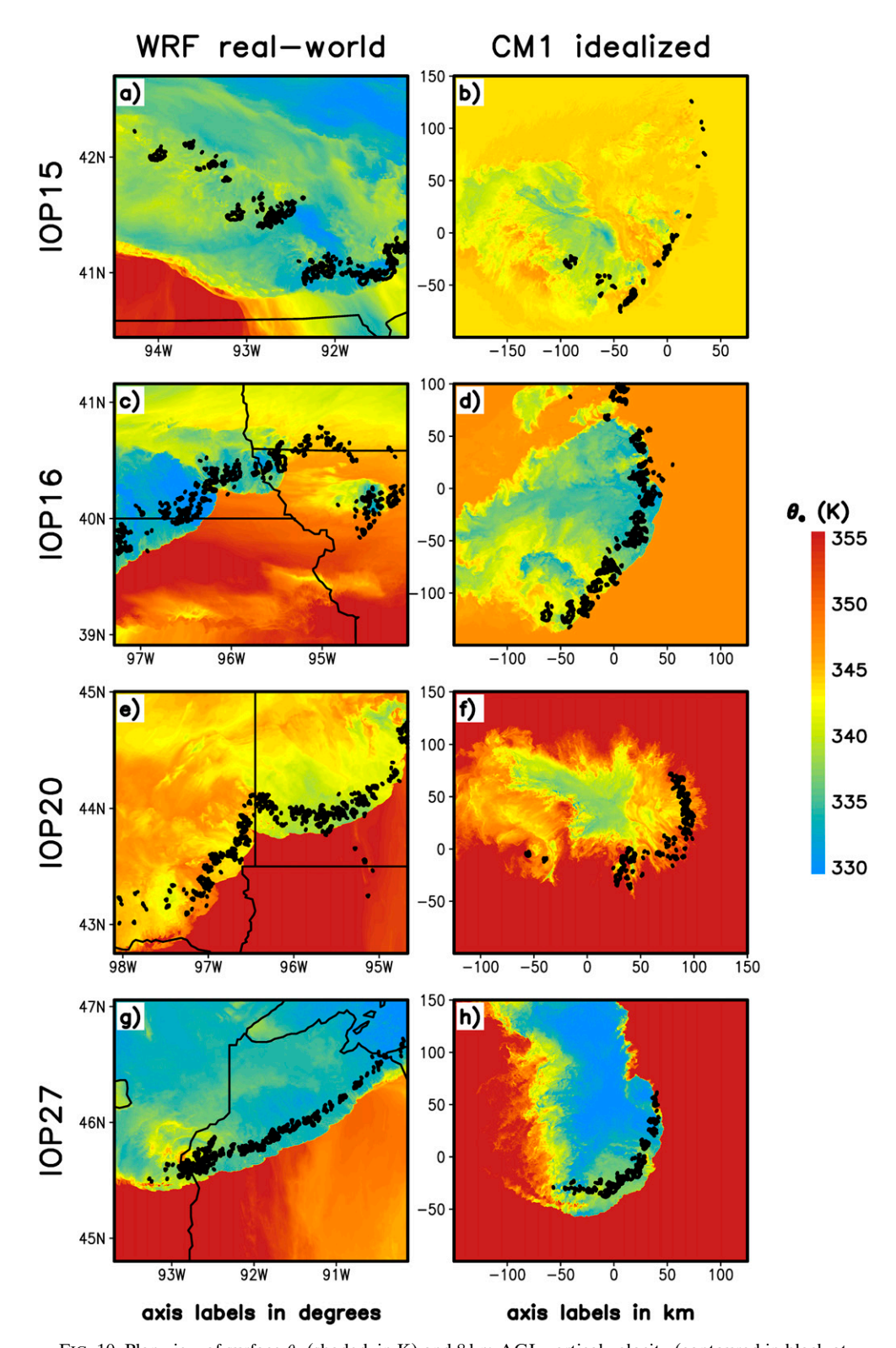


FIG. 10. Plan view of surface  $\theta_e$  (shaded, in K) and 8 km AGL vertical velocity (contoured in black at  $10\,\mathrm{m\,s^{-1}}$ ). All panels are valid for the same areas and times as their counterparts in Figs. 7–9.

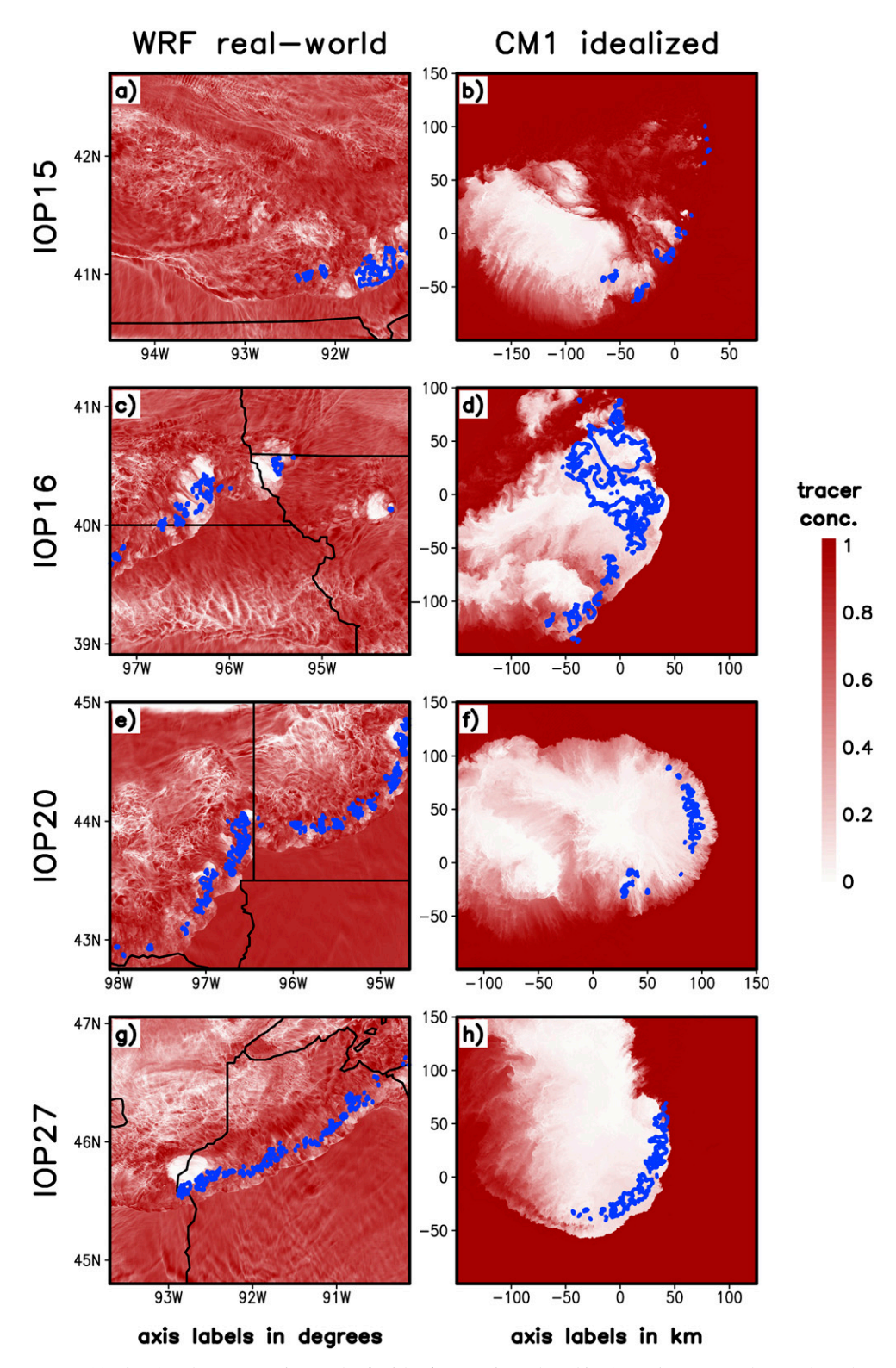


FIG. 11. Simulated concentration of the (unitless) tracer introduced in the  $0-500\,\mathrm{m}$  AGL layer, plotted at the surface (shaded as shown) and as a column maximum in the  $5-10\,\mathrm{km}$  AGL layer (contoured in blue at a concentration of 0.20). Each of the WRF depictions occurs 25 min after the tracer reset procedure described in section 2a. All panels are valid for the same areas and times as their counterparts in Figs. 7–10.

IOP15 this only occurs in the leading bowing segment (in both WRF and CM1; Figs. 11a,b), where the surface cold pool is most pronounced (e.g., Figs. 8 and 9). In contrast, the ROD segment extending to the northwest shows no deep lifting of surface tracer, and would therefore be considered elevated convection. This again resembles the findings of Hitchcock and Schumacher (2020) and will be discussed momentarily. For the other three cases, almost the entirety of each system's leading edge reveals gust front lifting of surface air into the middle and upper troposphere (Figs. 11c-h). In the environments with more SBCAPE and less SBCIN (IOPs 20 and 27; cf. Fig. 3), this behavior is at its most prolific, adding even more persuasive evidence to our motivating claim: "taken altogether, it appears that severe nocturnal MCSs may often resemble their cold pool-driven, surface-based afternoon counterparts" (P20, p. 183).

With the existence of surface outflows and ingestion of surface air now established, we finally return to the macroscale orientation of the self-organizing (CM1) systems. As shown in Fig. 4 (with shear and mean wind vectors shown in columns 1 and 3), the QLCS structures (convective lines or arcs, including bowing segments) are generally located toward the downshear side of the outflows. This fits with the general predictions for cold pool-driven systems by Rotunno et al. (1988). However, there are also segments of the MCSs that appear to continually develop into the low-level environmental flow (magenta vectors in Fig. 4), particularly the ROD segment in IOP15 (Figs. 4a,c) and the segment of CM1's IOP27 MCS that extends toward the west-northwest (Fig. 40). This windward face of an outflow is both a zone of general upglide (e.g., French and Parker 2010; Trier et al. 2010; Peters and Schumacher 2015) and a secondary location where more upright ascent occurs (e.g., Liu and Moncrieff 1996). The idealized (CM1) MCS orientations are therefore linked to both the system outflow and the ambient wind profile, and they appear to explain the self-organized aspects of the full-physics case study (WRF) simulated structures. We next ask whether these similar appearances are reflected in the MCS's finer-scale structures.

## b. Vertical structures

In creating a longitudinal review of eight simulations, by necessity there are fewer details presented from each individual run. The plan views in Figs. 7–11 encapsulate the system-scale structures during each simulated system's mature stage, and together support the important roles of cold pools in both self-organization and the evolution to surface-based convection. To move beyond this overview, we next examine the details of each system via vertical cross sections through representative segments of each simulated MCS. The position of each cross section is reflected by the blue lines in Fig. 7.

We begin with cross section A through the bowing segment of the IOP15 simulations (Fig. 12). As a reminder, this case has the lowest SBCAPE, the largest SBCIN, and the largest surface value of  $\Delta z_{\rm LFC}$  (Fig. 3), along with the strongest nearground stable layer (Fig. 2a). Much as shown in Figs. 8, 9a, and 9b, the WRF simulation shows a clear, well-developed surface cold pool (Fig. 12e); in contrast, the CM1 simulation reveals only a very shallow dome of cold air at the surface, and primarily

exhibits a wave or bore-like structure in the 0-1.5 km AGL layer (Fig. 12f). Nevertheless, as in Figs. 11a and 11b, both models show a lack of the "underflow" regime that Parker (2008) argued was indicative of elevated convection. This is revealed by the storm-relative inflow from the right side of both cross sections, which is linked to an ascending flow branch (rather than passing underneath the convective region; Figs. 12a,b) as well as by the stagnation and upward displacement of the surface tracer (Figs. 12c,d). This picture is completed by the presence of surface tracer in the midlevel updrafts of both simulations (shading within the black updraft contours in Figs. 12c,d). Not surprisingly, because it has a deeper cold pool, the upward tracer displacements are more substantial in the WRF realization. The pattern of tracer evolution shown in the CM1 cross section for IOP15 instead suggests a low-level layer that stagnates and deepens as would be expected in a bore (Fig. 12d); a much smaller fraction of this air makes it into the midlevels, so the CM1 representation is on the knife's edge between being surface based and totally elevated. The bowing segment of IOP15 appears to be the most dissimilar (WRF versus CM1) among the cross sections presented here. Even so, the cross sections through it reveal some rather classical signatures of self-organization and surface air lifting associated with its low-level outflow.

IOP15 is distinctive in that it comprises both the rapidly moving bowing segment as well as a more quasi-stationary zone of ROD. As analyzed in great detail by Hitchcock and Schumacher (2020), one of the most prevalent signatures in the IOP15B cross sections of potential temperature surfaces is the existence of an intrusion (annotated in Figs. 13e,f). This is a layer of outflow above the surface, visible as a zone of cooling above warming (to the left of  $x^* = 60 \text{ km}$  in Figs. 13e,f) that is due to deepening of that isentropic layer (in other words, a vertical spreading of the potential temperature surfaces). The fact that an intrusion occurs instead of a surface cold pool is likely a primary reason that the midlevel updrafts of the ROD segment are devoid of surface air (the lack of shading inside the black updraft contours in Figs. 13c,d; see also the lack of blue contours there in Figs. 11a,b). The primary storm-relative inflow is seen in the 0.5–2 km layer (from the left in Figs. 13a,b) and it is this elevated airstream that is primarily fueling the deep convection as it ascends the gently sloping potential surfaces seen above 0.5 km AGL in Figs. 13e and 13f. In short, the ROD segment of the IOP15 simulated MCSs comprises elevated convection, making it a useful counterpoint to the other four cross sections presented here. As is typical of elevated ROD convection, the deep convective cells occur well to the cold side of the surface outflow boundary (e.g., the surface  $\theta_e$  gradient in Figs. 10a,b).

P20 found that integrated precipitation was an important factor in determining where a surface cold pool eventually formed in simulations of IOP16. Here in IOP15, the difference between the leading edge outflow (Fig. 12) and the trailing ROD region may have primarily to do with the more uniform coverage and higher precipitation rates found in the bowing segment (e.g., Figs. 7a,b). In turn, these differences may be linked to the orientation of the low-level shear. The 0–3 and 0–6 km vector wind differences in the IOP15 environment

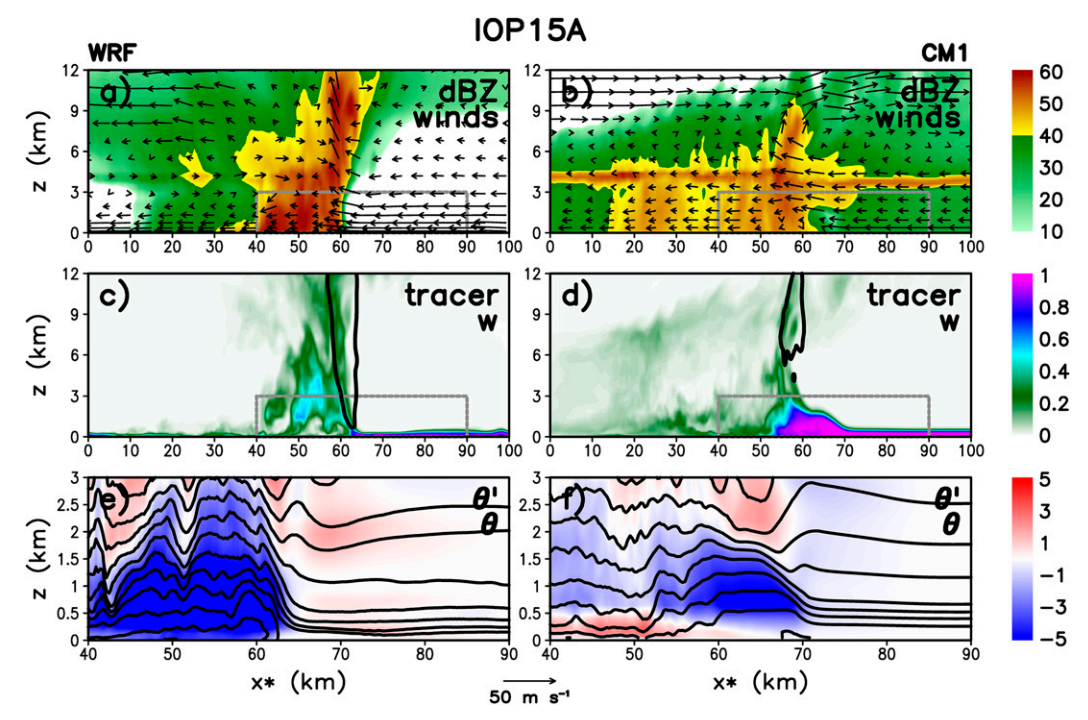


FIG. 12. Depiction of selected fields for cross sections "A" through the bow echo segment of the IOP15 MCS simulations. Data are from (left) 0525 UTC of the WRF simulation and (right)  $t = 4 \, h \, 0$  min of the CM1 simulation: (a),(b) vertical cross section of logarithmic radar reflectivity (shaded, in dBZ) and vectors for the wind components lying within the cross section (m s<sup>-1</sup>, scaled via reference vector at bottom); (c),(d) passive tracer concentrations originating from the 0–500 m AGL layer, with vertical velocity contoured in black at  $10 \, \text{m s}^{-1}$ ; (e),(f) vertical cross section of potential temperature perturbation (shaded, in K) and potential temperature (contoured every 2 K). These panels are valid at the same times as their counterparts in panels (a) and (b) in Figs. 7–11, with the position of the cross sections denoted in Figs. 7a and 7b by blue lines labeled "A." All fields in the vertical cross sections are averaged over a 5-km-wide horizontal swath that is centered on this line. All axis labels are in km; the *x*-axis values are distance along the cross section. To show detail, the horizontal and vertical axes are zoomed in (e) and (f). The area of the zoomed region is shown by a dashed gray box in (a)–(d).

are oriented toward the east/southeast (blue vectors in Figs. 4a,c). The component of shear that is perpendicular to the southeastward-moving bowing segment is directed away from the outflow (this outflow can be seen in panels a-b of Figs. 8–11 as well as the cross sections in Fig. 12). In contrast, along the ROD segment the vertical wind shear vectors point toward the outflow (this can be seen in Figs. 4a,c and 13a,b). A measure of the ratio between cold pool strength (represented by its theoretical speed, C, as in Rotunno et al. 1988) and lowertropospheric line-normal vertical wind shear (called  $\Delta u$ , as in Rotunno et al. 1988), reveals a near balance at the system's leading edge (IOP15A in Table 2 has a  $C/\Delta u \approx 1$ ) which has historically been argued to optimize gust front lifting. For the ROD segment,  $\Delta u < 0$  instead, providing a far from optimal situation for low-level lifting. Thus, instead of deep gust front ascent, the ROD segment develops where ambient flow (e.g., the magenta vectors in Figs. 4a,c) gradually glides up over the sloped isentropes (as also argued by Peters and Schumacher 2015; Hitchcock and Schumacher 2020). This combination of processes explains how the complex IOP15 structure is self-organized.

The cross sections for IOP16 are shown for completeness and comparison (Fig. 14), although a more detailed analysis

(including cross sections at multiple times) has already been provided by P20. The WRF and CM1 realizations are quite similar to one another. Even though the mean lower-tropospheric CAPE is the lowest among the four cases (i.e., the 0–1.5 km layer in Fig. 3a), the simulated systems exhibit clear surface cold pools (Figs. 14e,f) and clear lifting of surface tracer into the deep updrafts (Figs. 14c,d). The present article was largely motivated by the question of how generally these simulated IOP16 structures might apply to other nocturnal MCSs. As discussed above, they are at least partly evident in the downshear bowing segment of IOP15 (Fig. 12). We next turn to the other remaining cases.

Much as for IOP16, the cross sections through the IOP20 simulations reveal clear cold pools, with the WRF's again being stronger (Figs. 15e,f). And, again, the system appears to be surface-based given the upward displacement of tracer at the outflow boundary into the midlevels (Figs. 15c,d) and the lack of an underflow regime in the low-level winds (Figs. 15a,b). Perhaps the most surprising thing about the IOP20 simulations is that they do not look resoundingly surface based in the tracer cross sections (Figs. 15c,d); the lifting of the surface tracer is shallower and more sporadic than in the IOP16

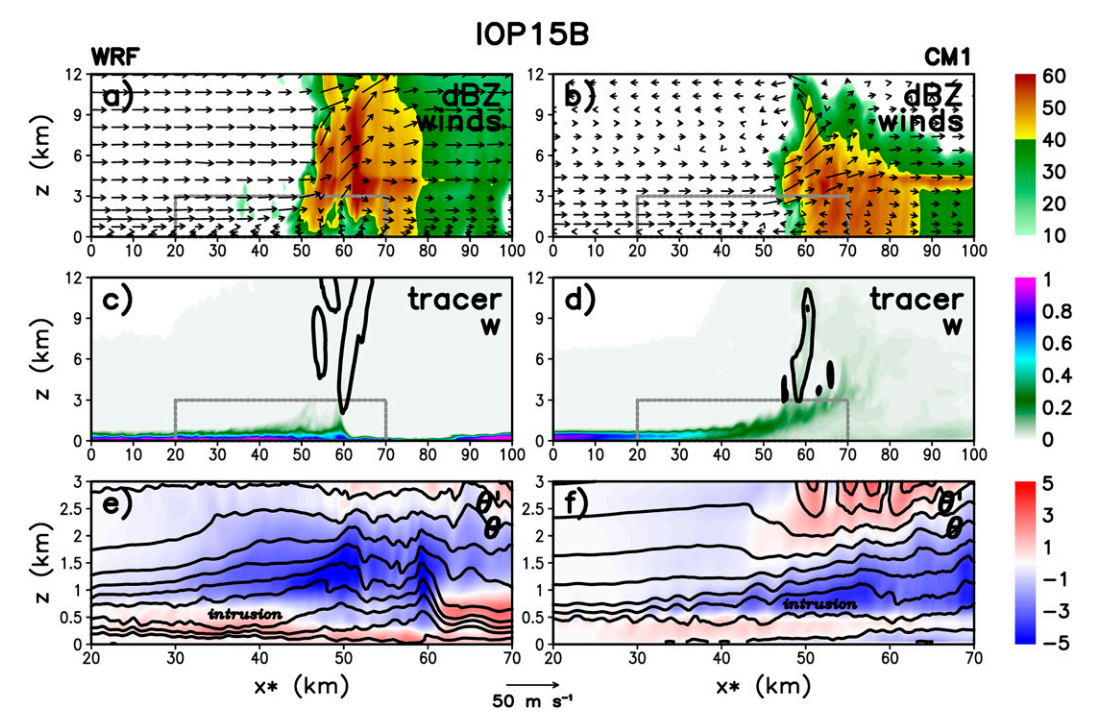


FIG. 13. As in Fig. 12, but for cross sections "B" through the ROD segment of the IOP15 MCS simulations. These panels are valid at the same times as their counterparts in panels (a) and (b) in Figs. 7–11, with the position of the cross sections denoted in Figs. 7a and 7b by blue lines labeled "B." The general location of the intrusion structure (discussed in the text) is annotated.

simulations (cf. Figs. 14c,d). The IOP20 case has more CAPE and less CIN than IOP16 at essentially every vertical level in the lower troposphere (Figs. 3a,b), with much smaller values of  $\Delta z_{\rm LFC}$  (Fig. 3c). Notably, the ambient lower-tropospheric vertical wind shear in the IOP20 environment is among the lowest of the four cases studied here (Table 2 as well as the blue vectors in Fig. 4). Even as the environment evolves over time within the simulations, the resulting ratio of  $C/\Delta u$  in the cross section ends up being rather far from what Rotunno et al. (1988) find as the optimal value of 1 (Table 2). Values of  $C/\Delta u$  well above 1 often correspond to QLCSs whose updraft regions slope strongly rearward over their cold pools, a behavior which does seem to be exhibited in the IOP20 cross sections (Figs. 15a,b). This seems to have produced a weaker system than CAPE alone might portend.

We conclude with the simulations of IOP27, for which the WRF and CM1 cross sections are the most similar of any examined here (Fig. 16). As for IOP16 and IOP20, there is a very clear surface cold pool (Figs. 16e,f), with very clear lifting of the surface tracer at the gust front and high concentrations of tracer found in the middle and upper-tropospheric updrafts (Figs. 16c,d). This system is the most definitively surface based and looks the most like a classical afternoon MCS in its cross-sectional view. This is likely due to the combination of high CAPE, the lowest 0–500 m averaged CIN, and the smallest 0–500 m averaged  $\Delta z_{\rm LFC}$  among the four environments (Fig. 3), along with only a very shallow weakly stable near-surface layer (Fig. 2d). The deep, cold outflow can be attributed to the

combination of high CAPE (favoring strong updrafts and large precipitation mass) and the layer of dry air residing not far aloft (between 850 and 600 hPa in Fig. 2d). These factors combine to produce the largest cold pool *C* values for both the WRF and

TABLE 2. Computed cold pool strength (C, m s<sup>-1</sup>), lower-tropospheric line-perpendicular vertical wind shear ( $\Delta u$ , m s<sup>-1</sup>), and their ratio ( $C/\Delta u$ , unitless) from the cross sections shown in Figs. 12–16. In each case, the calculations are performed using 5 km averages (in the along-line direction) centered on the cross section (the same procedure used in making Figs. 12–16). The value of C is computed following Rotunno et al. (1988), using integration over the layer 0–3 km AGL, averaged over a 20 km window within the cold pool (centered upon the location of maximum C) omitting any points where C is undefined (i.e., where there are warm anomalies). The value of  $\Delta u$  is computed as the difference between the maximum line-normal wind found between 0 and 3 km AGL and the minimum (or most negative) line-normal wind found at a level below it, averaged over the 20 km window of the cross section that is farthest from the convection on its inflow side.

Cross section	WRF simulation			CM1 simulation		
	С	$\Delta u$	$C/\Delta u$	С	$\Delta u$	C/\Delta u
IOP15A (Fig. 12)	24.8	22.2	1.1	15.3	13.2	1.2
IOP15B (Fig. 13)	16.9	-25.7	-0.7	15.0	-25.5	-0.6
IOP16 (Fig. 14)	27.2	17.8	1.5	23.8	24.6	1.0
IOP20 (Fig. 15)	27.4	16.9	1.6	16.1	10.7	1.5
IOP27 (Fig. 16)	31.5	10.9	2.9	24.1	16.9	1.4

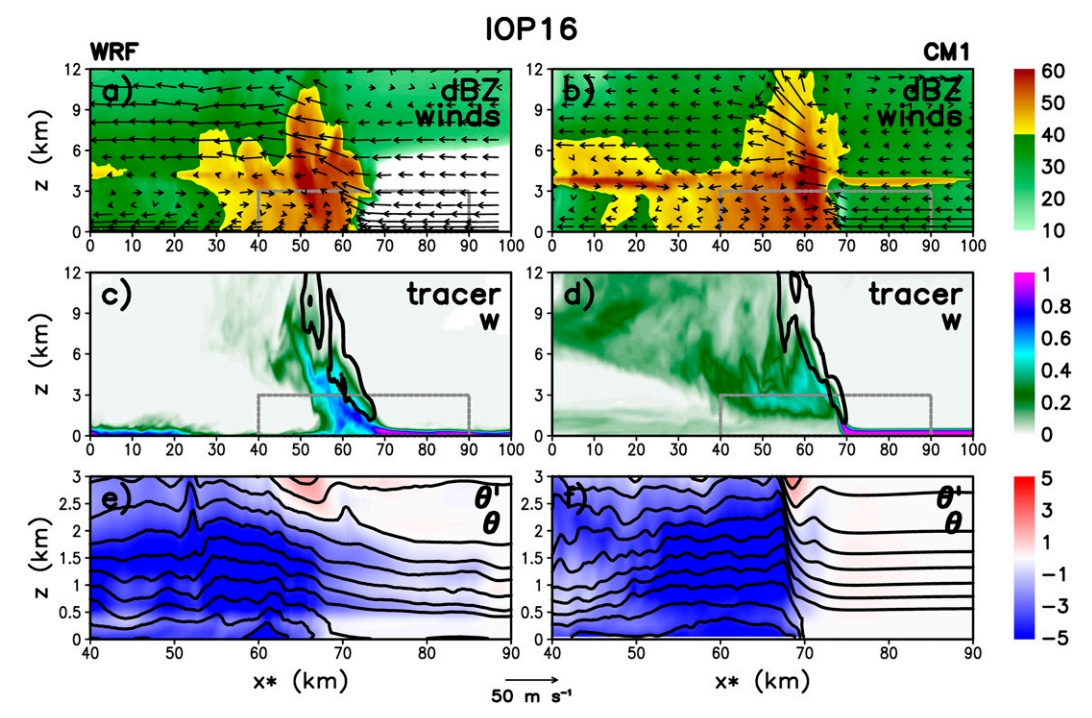


FIG. 14. As in Fig. 12, but for cross sections through the IOP16 MCS at (left) 0555 UTC from the WRF simulation and (right) t = 4 h 0 min from the CM1 simulation. These panels are valid at the same times as their counterparts in panels (c) and (d) in Figs. 7–11, with the position of the cross sections denoted in Figs. 7c and 7d by blue lines.

CM1 suites (Table 2). This in turn contributes to  $C/\Delta u$  values well above 1, as in IOP20, which again is consistent with the strong sloping of the main ascending flow branch rearward over the cold pool (Figs. 16a,b). The WRF simulation in particular combines a very strong cold pool with rather weak lowertropospheric shear (Table 2), which might be regarded as far from optimal for convective retriggering. However, it is clear that the WRF cold pool is easily 2–3 km deep (Fig. 16e), and the required vertical displacements for low-level air parcels to reach their LFCs are 1500 m or less, with some parcels in the 500-1000 m AGL layer requiring less than 300 m of lifting (Fig. 3c). In other words, once a strong deep cold pool is established, the lifting does not need to be optimal (from the perspective of the theory of Rotunno et al. 1988); its depth merely needs to be sufficient for air parcels to be raised to their LFCs (a similar point to that made by Stensrud et al. 2005).

The value of these eight simulations is in the commonalities that emerge across the sample. Although the details vary between models and between cases, it appears that all four nocturnal events are consistent with the existence of at least some surface outflow that is accompanied by lifting of near-surface air into deep updrafts. Evidence that the convective systems become surface based includes the upward displacement of surface tracers as well as the cessation of the underflow regime that characterizes elevated convection. The similarities between the WRF and CM1 simulations, both in terms of gross evolution and in terms of cross sectional details, suggest that a substantial component of the simulated MCS behavior is self-organized (i.e.,

not reliant on larger-scale features external to the convection). P20 arrived at similar conclusions based on a study of IOP16 alone; the fact that the other three cases simulated here exhibit common features and processes suggests that their results are more general. At least for a prominent subset of cases (here, among the most well organized and severe from PECAN), there is evidence that nocturnal MCSs resemble traditional daytime systems, with self-organization via cold pool processes and subsequent evolution to lifting of surface air at the leading outflow boundary.

## 5. Conclusions

Advancing our understanding of recurring processes in nocturnal MCSs was a principal goal of the PECAN field project, four cases from which are the backbone of the present work. Are nocturnal MCSs generally self-organizing? If so, by what processes do they self-organize? Are these the same processes that allow diurnal MCSs to self-organize? Our approach to addressing these questions was an integrative study of the four nocturnal MCSs, each simulated at two different levels of complexity (real-world-like case study simulations using WRF vs idealized simulations using CM1).

## a. Primary findings

Each MCS has a unique environment, evolution, and structure. Rather than focusing on what distinguishes these MCSs from one another, we viewed the suite of eight simulations

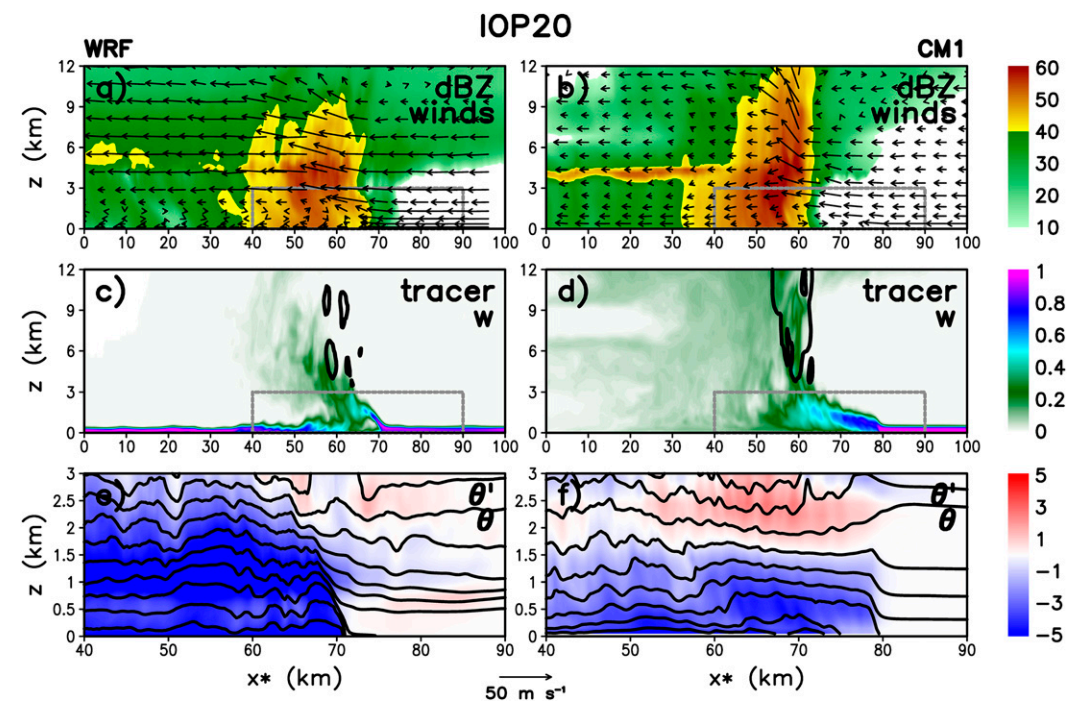


FIG. 15. As in Fig. 12, but for cross sections through the IOP20 MCS at (left) 0455 UTC from the WRF simulation and (right) t = 4 h 0 min from the CM1 simulation. These panels are valid at the same times as their counterparts in panels (e) and (f) in Figs. 7–11, with the position of the cross sections denoted in Figs. 7e and 7f by blue lines.

longitudinally to identify common properties and processes. The most important cross-cutting findings are the following.

- Not surprisingly, the case study (WRF) simulations generally look more like the observed cases than the idealized (CM1) simulations. Nevertheless, the verisimilitude of the idealized MCSs (in horizontally homogeneous environments) suggests that a substantial component of the studied cases was self-organized (i.e., determined by the environment and history of the MCS itself, as opposed to external large-scale heterogeneity or ascent). In this way of thinking, the primary role of the synoptic scale would be to prearrange the local thermodynamic and wind profiles within which the MCS subsequently occurs.
- All of the nocturnal MCS simulations produce outflows in the form of surface cold pools. This finding, combined with the PECAN observations presented by Hitchcock et al. (2019), indicates that many (perhaps most) nocturnal MCSs produce cold pools. These cold pools form via low level in situ evaporation in some cases, but all of the simulated cold pools also included midlevel air (with lower θ<sub>e</sub>) from aloft. Simulated cold pools are generally stronger (in terms of temperature deficit and depth) in the environments with more CAPE and weaker near-ground static stability. Cold pools are also stronger in the case study (WRF) simulations than in the idealized (CM1) simulations, which may mean that cold pools' roles in self-organization of nocturnal MCSs are actually underdone in the idealized simulations.

 As cold pools emerge, the simulated systems exhibit lifting of near-ground tracers into midlevel updrafts along with a lack of the underflow regime that typifies elevated convective systems (e.g., Parker 2008). In short, all simulated MCSs eventually become at least partly surface based. At this point, the systems all have classical QLCS structures, including convective lines (often with bow echo structures) toward the downshear edges of their cold pools.

Altogether, the assertions of P20 apply to this somewhat larger sample of simulated cases: well-organized nocturnal squall lines appear to share many attributes of their daytime counterparts.

The primary strength of the present approach is in identifying recurring behaviors among the ensemble of simulations. But we also note that the rather distinctive 24–25 June 2015 ("IOP15") simulations produce a complex, realistic structure with both a bowing segment and an observed zone of rearward off-boundary development (Peters and Schumacher 2014). That such evolution can be captured in a horizontally homogeneous environment is further evidence that a wide range of nocturnal MCS structures may indeed be self-organized.

It is finally of interest to note that each of the four nocturnal MCSs studied here was observed to produce severe surface winds. Although there is prior evidence in the literature that truly elevated MCSs can produce severe winds (e.g., Bosart and Seimon 1988; Schmidt and Cotton 1989; Knupp 1996; Bernardet and Cotton 1998), it may well be that nocturnal MCSs producing severe surface winds are often surface-based

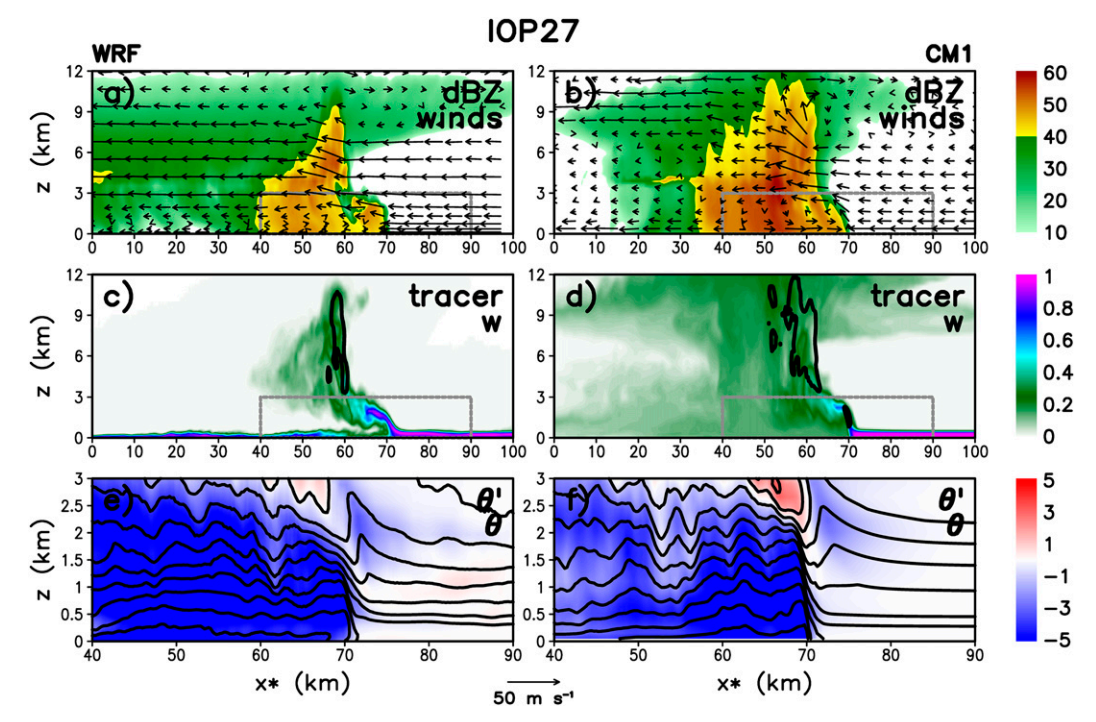


FIG. 16. As in Fig. 12, but for cross sections through the IOP27 MCS at (left) 0725 UTC from the WRF simulation and (right) t = 4 h 0 min from the CM1 simulation. These panels are valid at the same times as their counterparts in panels (g) and (h) in Figs. 7–11, with the position of the cross sections denoted in Figs. 7g and 7h by blue lines.

(and producing severe winds via classical downdraft and outflow mechanisms). This hypothesis finds additional support in the recent study by Mauri and Gallus (2021), wherein higher surface-based and mixed-layer CAPE values appear to be meaningfully related to severe wind production by nocturnal bow echoes.

## b. Future work

Sensitivities to numerical model configurations can always be explored further. Although such statements are rather customary, the apparent importance of evaporatively developed cold pools in these simulations implies that further examination of optimal model microphysical parameterizations may be particularly worthwhile. Such experiments could be revealing in environments like IOP15 that only marginally support cold pool formation. As noted by Parsons et al. (2019), subtle changes in cold pool strength can then also alter the probability of flow blocking and bores (represented by the fluid depth and Froude number parameter space). A better understanding of model microphysical sensitivities might in turn help to enhance operations via better configuration of convection-allowing model (CAM) numerical weather predictions. Indeed, it would be worthwhile to perform an audit of the quality of CAM forecasts across a wide range of cases. CAM guidance was used heavily in the daily PECAN forecasting process, but Stelten and Gallus (2017) subsequently showed that these CAMs were not particularly skillful in terms of the initial timing and location of MCS development. It is unknown how well presently operational CAMs represent the evolutionary pathways identified in the current study. Beyond numerical models, it would be extremely beneficial to conduct longitudinal studies (similar to this one) using direct observations. Such a cross-cutting synthesis will be challenging given the diversity and complexity of data from field campaigns like PECAN. Nevertheless, consolidating the advances in our understanding probably provides the most direct route to improvements in how forecasters use environmental information to anticipate nocturnal MCS hazards and impacts (e.g., severe winds, as in all cases here, and flash flooding, as in IOP15).

Overall, a much broader spectrum of nocturnal MCSs requires continued study; one should not conclude from the present study that all MCSs are identical. As reviewed in section 3, the present cases represent PECAN MCS environments well, but span a rather small part of the parameter space. The cases studied here were also among the strongest and bestorganized from PECAN, so perhaps other nocturnal MCSs with lower precipitation rates have a lesser propensity to produce cold pools. All of the present nocturnal MCS cases also occurred in summer environments that had weak-moderate synoptic-scale lifting and possessed non-zero surface-based CAPE, so it is possible that this subset of MCSs represents the most afternoon-like of the population of nocturnal systems. There is almost certainly a subclass of nocturnal MCSs that are more strongly externally organized (vs self-organized) and that remain elevated. Such systems may occur in the cooler seasons within environments lacking surface-based CAPE (often on the cool side of warm or stationary fronts). This alternative subclass perhaps conforms more closely to historical expectations of nocturnal systems, but is certainly worthy of further study.

Finally, there are of course still differences between the four environments studied here and true afternoon convective environments (which commonly have less low-level vertical wind shear and lack near-ground stable layers). It would be of interest to examine how much those differences matter to the overall structure and evolution of seemingly similar cold pool–driven MCSs. A detailed sensitivity study could add nuance to the most important present finding, which is that many nocturnal MCSs bear strong resemblance to their diurnal counterparts.

Acknowledgments. George Bryan is gratefully acknowledged for providing and supporting the CM1. Stacey Hitchcock provided some valuable insights and techniques for the IOP15 case. This work was supported by the National Science Foundation under Grant AGS-1359709. Simulations were accomplished with high-performance computing support from Yellowstone (ark:/85065/d7wd3xhc) and Cheyenne (doi:10.5065/D6RX99HX) provided by NCAR's Computational and Information Systems Laboratory, sponsored by the National Science Foundation. The author thanks the members of the NCSU Convective Storms Group for their beneficial comments, and the many field workers from the PECAN campaign for their late night travail in acquiring the observational data.

Data availability statement. The CM1 model code is available from https://www2.mmm.ucar.edu/people/bryan/cm1/. The WRF model code is available from https://www2.mmm.ucar.edu/wrf/users/downloads.html. PECAN soundings data are available from http://dx.doi.org/10.5065/D6W66HXN. All other namelists, input files, and postprocessing scripts are available from the author by request.

## REFERENCES

- Bernardet, L. R., and W. R. Cotton, 1998: Multiscale evolution of a derecho-producing mesoscale convective system. *Mon. Wea. Rev.*, **126**, 2991–3015, https://doi.org/10.1175/1520-0493(1998) 126<2991:MEOADP>2.0.CO;2.
- Billings, J. M., and M. D. Parker, 2012: Evolution and maintenance of the 22–23 June 2003 nocturnal convection during BAMEX. Wea. Forecasting, 27, 279–300, https://doi.org/10.1175/WAF-D-11-00056.1.
- Bodine, D. J., and K. L. Rasmussen, 2017: Evolution of mesoscale convective system organizational structure and convective line propagation. *Mon. Wea. Rev.*, 145, 3419–3440, https://doi.org/ 10.1175/MWR-D-16-0406.1.
- Bosart, L. F., and A. Seimon, 1988: A case study of an unusually intense atmospheric gravity wave. *Mon. Wea. Rev.*, 116, 1857–1886, https://doi.org/10.1175/1520-0493(1988)116<1857: ACSOAU>2.0.CO;2.
- Bryan, G. H., and J. M. Fritsch, 2002: A benchmark simulation for moist nonhydrostatic numerical models. *Mon. Wea. Rev.*, 130, 2917–2928, https://doi.org/10.1175/1520-0493(2002)130<2917: ABSFMN>2.0.CO;2.
- —, and M. D. Parker, 2010: Observations of a squall line and its near environment using high-frequency rawinsonde launches during VORTEX2. *Mon. Wea. Rev.*, **138**, 4076–4097, https://doi.org/10.1175/2010MWR3359.1.
- —, and H. Morrison, 2012: Sensitivity of a simulated squall line to horizontal resolution and parameterization of microphysics.

- Mon. Wea. Rev., **140**, 202–225, https://doi.org/10.1175/MWR-D-11-00046.1.
- Carbone, R. E., J. D. Tuttle, D. A. Ahijevych, and S. B. Trier, 2002: Inferences of predictability associated with warm season precipitation episodes. J. Atmos. Sci., 59, 2033–2056, https://doi.org/ 10.1175/1520-0469(2002)059<2033:IOPAWW>2.0.CO;2.
- Chen, F., and J. Dudhia, 2001: Coupling an advanced land surface-hydrology model with the Penn State–NCAR MM5 modeling system. Part I: Model implementation and sensitivity. *Mon. Wea. Rev.*, **129**, 569–585, https://doi.org/10.1175/1520-0493(2001) 129<0569:CAALSH>2.0.CO;2.
- Chipilski, H. G., X. Wang, and D. B. Parsons, 2020: Impact of assimilating PECAN profilers on the prediction of bore-driven nocturnal convection: A multiscale forecast evaluation for the 6 July 2015 case study. *Mon. Wea. Rev.*, 148, 1147–1175, https://doi.org/10.1175/MWR-D-19-0171.1.
- Colman, B. R., 1990: Thunderstorms above frontal surfaces in environments without positive CAPE. Part I: A climatology. *Mon. Wea. Rev.*, **118**, 1103–1122, https://doi.org/10.1175/1520-0493(1990)118<1103:TAFSIE>2.0.CO;2.
- Davis, C. A., K. W. Manning, R. E. Carbone, S. B. Trier, and J. D. Tuttle, 2003: Coherence of warm-season continental rainfall in numerical weather prediction models. *Mon. Wea. Rev.*, 131, 2667–2679, https://doi.org/10.1175/1520-0493(2003)131<2667: COWCRI>2.0.CO;2.
- Deardorff, J. W., 1980: Stratocumulus-capped mixed layers derived from a three-dimensional model. *Bound.-Layer Meteor.*, **18**, 495–527, https://doi.org/10.1007/BF00119502.
- Degelia, S. K., X. Wang, and D. J. Stensrud, 2019: An evaluation of the impact of assimilating AERI retrievals, kinematic profilers, rawinsondes, and surface observations on a forecast of a nocturnal convection initiation event during the PECAN field campaign. *Mon. Wea. Rev.*, 147, 2739–2764, https://doi.org/ 10.1175/MWR-D-18-0423.1.
- Dudhia, J., 1989: Numerical study of convection observed during the Winter Monsoon Experiment using a mesoscale two-dimensional model. J. Atmos. Sci., 46, 3077–3107, https://doi.org/10.1175/ 1520-0469(1989)046<3077:NSOCOD>2.0.CO;2.
- Flournoy, M. D., and M. C. Coniglio, 2019: Origins of vorticity in a simulated tornadic mesovortex observed during PECAN on 6 July 2015. *Mon. Wea. Rev.*, **147**, 107–134, https://doi.org/10.1175/MWR-D-18-0221.1.
- Fovell, R. G., and Y. Ogura, 1988: Numerical simulation of a midlatitude squall line in two dimensions. *J. Atmos. Sci.*, **45**, 3846–3879, https://doi.org/10.1175/1520-0469(1988)045<3846: NSOAMS>2.0.CO;2.
- French, A. J., and M. D. Parker, 2010: The response of simulated nocturnal convective systems to a developing low-level jet. *J. Atmos. Sci.*, **67**, 3384–3408, https://doi.org/10.1175/2010JAS3329.1.
- Fritsch, J. M., and R. E. Carbone, 2004: Improving quantitative precipitation forecasts in the warm season. *Bull. Amer. Meteor. Soc.*, **85**, 955–966, https://doi.org/10.1175/BAMS-85-7-955.
- ——, R. J. Kane, and C. R. Chelius, 1986: The contribution of mesoscale convective weather systems to the warm-season precipitation in the United States. *J. Climate Appl. Meteor.*, 25, 1333–1345, https://doi.org/10.1175/1520-0450(1986)025<1333: TCOMCW>2.0.CO;2.
- Geerts, B., and Coauthors, 2017: The 2015 Plains Elevated Convection At Night Field Project. Bull. Amer. Meteor. Soc., 98, 767–786, https://doi.org/10.1175/BAMS-D-15-00257.1.
- Hitchcock, S. M., and R. S. Schumacher, 2020: Analysis of back-building convection in simulations with a strong low-level

- stable layer. *Mon. Wea. Rev.*, **148**, 3773–3797, https://doi.org/10.1175/MWR-D-19-0246.1.
- —, —, G. R. Herman, M. C. Coniglio, M. D. Parker, and C. L. Ziegler, 2019: Evolution of pre- and postconvective environmental profiles from mesoscale convective systems during PECAN. *Mon. Wea. Rev.*, **147**, 2329–2354, https://doi.org/10.1175/MWR-D-18-0231.1.
- Janjić, Z. I., 2002: Nonsingular implementation of the Mellor-Yamada level 2.5 scheme in the NCEP Meso model. NCEP Office Note 437, 61 pp., http://www.emc.ncep.noaa.gov/officenotes/ newernotes/on437.pdf.
- Kain, J. S., 2004: The Kain–Fritsch convective parameterization: An update. *J. Appl. Meteor.*, **43**, 170–181, https://doi.org/ 10.1175/1520-0450(2004)043<0170:TKCPAU>2.0.CO:2.
- —, and J. M. Fritsch, 1993: Convective parameterization for mesoscale models: The Kain–Fritsch scheme. *The Representation* of Cumulus Convection in Numerical Models, Meteor. Monogr., No. 46, Amer. Meteor. Soc., 165–170.
- Keene, K. M., and R. S. Schumacher, 2013: The bow and arrow mesoscale convective structure. *Mon. Wea. Rev.*, 141, 1648– 1672, https://doi.org/10.1175/MWR-D-12-00172.1.
- Klemp, J. B., W. C. Skamarock, and J. Dudhia, 2007: Conservative split-explicit time integration methods for the compressible nonhydrostatic equations. *Mon. Wea. Rev.*, 135, 2897–2913, https://doi.org/10.1175/MWR3440.1.
- Knupp, K. R., 1996: Structure and evolution of a long-lived, microburst-producing storm. *Mon. Wea. Rev.*, **124**, 2785–2806, https://doi.org/10.1175/1520-0493(1996)124<2785:SAEOAL>2.0.CO;2.
- Liu, C., and M. W. Moncrieff, 1996: A numerical study of the effects of ambient flow and shear on density currents. *Mon. Wea. Rev.*, **124**, 2282–2303, https://doi.org/10.1175/1520-0493(1996) 124<2282:ANSOTE>2.0.CO;2.
- Maddox, R. A., 1980: Mesoscale convective complexes. *Bull. Amer. Meteor. Soc.*, **61**, 1374–1387, https://doi.org/10.1175/1520-0477(1980)061<1374:MCC>2.0.CO;2.
- Mauri, E. L., and W. A. Gallus Jr., 2021: Differences between severe and nonsevere warm-season, nocturnal bow echo environments. Wea. Forecasting, 36, 53–74, https://doi.org/10.1175/WAF-D-20-0137.1.
- Mellor, G. L., and T. Yamada, 1982: Development of a turbulence closure model for geophysical fluid problems. *Rev. Geophys.*, 20, 851–875, https://doi.org/10.1029/RG020i004p00851.
- Miller, R. L., C. L. Ziegler, and M. I. Biggerstaff, 2020: Seven-Doppler radar and in situ analysis of the 25–26 June 2015 Kansas MCS during PECAN. Mon. Wea. Rev., 148, 211–240, https://doi.org/10.1175/MWR-D-19-0151.1.
- Mlawer, E. J., S. J. Taubman, P. D. Brown, M. J. Iacono, and S. A. Clough, 1997: Radiative transfer for inhomogeneous atmospheres: RRTM, a validated correlated-k model for the long-wave. J. Geophys. Res., 102, 16663–16682, https://doi.org/10.1029/97JD00237.
- Morrison, H., G. Thompson, and V. Tatarskii, 2009: Impact of cloud microphysics on the development of trailing stratiform precipitation in a simulated squall line: Comparison of oneand two-moment schemes. *Mon. Wea. Rev.*, 137, 991–1007, https://doi.org/10.1175/2008MWR2556.1.
- Newton, C. W., 1950: Structure and mechanism of the prefrontal squall line. *J. Meteor.*, **7**, 210–222, https://doi.org/10.1175/1520-0469(1950)007<0210:SAMOTP>2.0.CO;2.
- Olson, D. A., N. W. Junker, and B. Korty, 1995: Evaluation of 33 years of quantitative precipitation forecasting at the NMC. *Wea. Forecasting*, **10**, 498–511, https://doi.org/10.1175/1520-0434(1995)010<0498:EOYOQP>2.0.CO;2.

- Parker, M. D., 2008: Response of simulated squall lines to low-level cooling. J. Atmos. Sci., 65, 1323–1341, https://doi.org/10.1175/ 2007JAS2507.1.
- ——, 2014: Composite VORTEX2 supercell environments from near-storm soundings. *Mon. Wea. Rev.*, **142**, 508–529, https:// doi.org/10.1175/MWR-D-13-00167.1.
- ——, B. S. Borchardt, R. L. Miller, and C. L. Ziegler, 2020: Simulated evolution and severe wind production by the 25–26 June 2015 nocturnal MCS from PECAN. *Mon. Wea. Rev.*, 148, 183–209, https://doi.org/10.1175/MWR-D-19-0072.1.
- Parsons, D. B., K. R. Haghi, K. T. Halbert, B. Elmer, and J. Wang, 2019: The potential role of atmospheric bores and gravity waves in the initiation and maintenance of nocturnal convection over the Southern Great Plains. J. Atmos. Sci., 76, 43–68, https://doi.org/10.1175/JAS-D-17-0172.1.
- Peters, J. M., and R. S. Schumacher, 2014: Objective categorization of heavy-rain-producing MCS synoptic types by rotated principal component analysis. *Mon. Wea. Rev.*, **142**, 1716–1737, https://doi.org/10.1175/MWR-D-13-00295.1.
- ——, and ——, 2015: Mechanisms for organization and echo training in a flash-flood-producing mesoscale convective system. *Mon. Wea. Rev.*, **143**, 1058–1085, https://doi.org/10.1175/MWR-D-14-00070.1.
- —, E. R. Nielsen, M. D. Parker, S. M. Hitchcock, and R. S. Schumacher, 2017: The impact of low-level moisture errors on model forecasts of an MCS observed during PECAN. *Mon. Wea. Rev.*, 145, 3599–3624, https://doi.org/10.1175/MWR-D-16-0296.1.
- Rotunno, R., J. B. Klemp, and M. L. Weisman, 1988: A theory for strong, long-lived squall lines. *J. Atmos. Sci.*, 45, 463–485, https:// doi.org/10.1175/1520-0469(1988)045<0463:ATFSLL>2.0.CO;2.
- Schmidt, J. M., and W. R. Cotton, 1989: A High Plains squall line associated with severe surface winds. J. Atmos. Sci., 46, 281–302, https://doi.org/10.1175/1520-0469(1989)046<0281:AHPSLA> 2.0.CO;2.
- Skamarock, W. C., and J. B. Klemp, 2008: A time-split non-hydrostatic atmospheric model for weather research and forecasting applications. *J. Comput. Phys.*, 227, 3465–3485, https://doi.org/10.1016/j.jcp.2007.01.037.
- —, and Coauthors, 2008: A description of the Advanced Research WRF version 3. NCAR Tech. Note NCAR/TN-475+STR, 113 pp., https://doi.org/10.5065/D68S4MVH.
- Stelten, S., and W. A. Gallus Jr., 2017: Pristine nocturnal convective initiation: A climatology and preliminary examination of predictability. Wea. Forecasting, 32, 1613–1635, https://doi.org/10.1175/WAF-D-16-0222.1.
- Stensrud, D. J., M. C. Coniglio, R. P. Davies-Jones, and J. S. Evans, 2005: Comments on "A theory for strong long-lived squall lines' revisited." *J. Atmos. Sci.*, 62, 2989–2996, https://doi.org/ 10.1175/JAS3514.1.
- Thielen, J. E., and W. A. Gallus, 2019: Influences of horizontal grid spacing and microphysics on WRF forecasts of convective morphology evolution for nocturnal MCSs in weakly forced environments. *Wea. Forecasting*, **34**, 1495–1517, https://doi.org/10.1175/WAF-D-18-0210.1.
- Thompson, G., P. R. Field, R. M. Rasmussen, and W. D. Hall, 2008: Explicit forecasts of winter precipitation using an improved bulk microphysics scheme. Part II: Implementation of a new snow parameterization. *Mon. Wea. Rev.*, 136, 5095–5115, https://doi.org/10.1175/2008MWR2387.1.
- Thorpe, A. J., M. J. Miller, and M. W. Moncrieff, 1982: Two-dimensional convection in non-constant shear: A model of mid-latitude squall lines. *Quart. J. Roy. Meteor. Soc.*, 108, 739–762, https://doi.org/10.1002/qj.49710845802.

- Trier, S. B., C. A. Davis, and D. A. Ahijevych, 2010: Environmental controls on the simulated diurnal cycle of warm-season precipitation in the continental United States. *J. Atmos. Sci.*, 67, 1066–1090, https://doi.org/10.1175/2009JAS3247.1.
- Wallace, J. M., 1975: Diurnal variations in precipitation and thunderstorm frequency over the conterminous United States. *Mon. Wea. Rev.*, **103**, 406–419, https://doi.org/10.1175/1520-0493(1975)103<0406:DVIPAT>2.0.CO;2.
- Weisman, M. L., C. Davis, W. Wang, K. W. Manning, and J. B. Klemp, 2008: Experiences with 0–36 h explicit convective forecasts with the WRF-ARW model. *Wea. Forecasting*, 23, 407–437, https://doi.org/10.1175/2007WAF2007005.1.
- Zipser, E. J., 1977: Mesoscale and convective–scale downdrafts as distinct components of squall-line structure. *Mon. Wea. Rev.*, **105**, 1568–1589, https://doi.org/10.1175/1520-0493(1977) 105<1568:MACDAD>2.0.CO;2.